processes

MDPI

Article

Influence of Surface Roughness Modeling on the Aerodynamics of an Iced Wind Turbine S809 Airfoil

Leidy Tatiana Contreras Montoya [1,2], Adrian Ilinca [1,*] and Santiago Lain [2,*]

[1] Mechanical Engineering Department, Faculty of Engineering, École de Technologie Supérieure, University of Québec, Montreal, QC H3C 1K3, Canada; leidy-tatiana.contreras-montoya.1@ens.etsmtl.ca
[2] PAI+ Group, Energetics & Mechanics Department, Faculty of Engineering, Universidad Autonoma de Occidente, Cali 760030, Valle del Cauca, Colombia
* Correspondence: adrian.ilinca@etsmtl.ca (A.I.); slain@uao.edu.co (S.L.)

Abstract: Ice formation on structures like wind turbine blade airfoils significantly reduces their aerodynamic efficiency. The presence of ice on airfoils causes deformation in their geometry and an increase in their surface roughness, enhancing turbulence, particularly on the suction side of the airfoil at high angles of attack. An approach for understanding this phenomenon and assessing its impact on wind turbine operation is modeling and simulation. In this contribution, a computational fluid dynamics (CFD) study is conducted using FENSAP-ICE 2022 R1 software available in the ANSYS package. The objective was to evaluate the influence of surface roughness modeling (Shin et al. and beading models) in combination with different turbulence models (Spalart–Allmaras and k-ω shear stress transport) on the estimation of the aerodynamic performance losses of wind turbine airfoils not only under rime ice conditions but also considering the less studied case of glaze ice. Moreover, the behavior of the commonly less explored pressure and skin friction coefficients is examined in the clean and iced airfoil scenarios. As a result, the iced profile experiences higher drag and lower lift than in the no-ice conditions, which is explained by modifying skin friction and pressure coefficients by ice. Overall, the outcomes of both turbulence models are similar, showing maximum differences not higher than 10% in the simulations for both ice regimes. However, it is demonstrated that the influence of blade roughness was critical and cannot be disregarded in ice accretion simulations on wind turbine blades. In this context, the beading model has demonstrated an excellent ability to manage changes in roughness throughout the ice accretion process. On the other hand, the widely used roughness model of Shin et al. could underestimate the lift and overestimate the drag coefficients of the wind turbine airfoil in icy conditions.

Keywords: turbulent flow; rime and glaze ice; wind turbine rough surface; CFD simulation; aerodynamic loss

Citation: Contreras Montoya, L.T.; Ilinca, A.; Lain, S. Influence of Surface Roughness Modeling on the Aerodynamics of an Iced Wind Turbine S809 Airfoil. *Processes* **2023**, *11*, 3371. https://doi.org/10.3390/pr11123371

Academic Editor: Michael C. Georgiadis

Received: 28 October 2023
Revised: 23 November 2023
Accepted: 28 November 2023
Published: 5 December 2023

1. Introduction

Simulation and modeling techniques have become increasingly valuable in studying and analyzing ice accretion on wind turbines. These methods offer numerous advantages compared to experimental approaches, including cost-effectiveness, efficiency, and the ability to explore diverse icing events. Nonetheless, achieving accurate ice accretion modeling on wind turbines demands a comprehensive approach involving multiple disciplines, encompassing thermodynamics, aerodynamics, heat transfer, and mass transfer.

Computer-aided engineering techniques are commonly utilized to conduct these analyses, employing various tools and approaches for numerically solving coupled differential equations through finite element and finite volume methods [1–3]. Additionally, emerging methodologies such as deep learning, genetic algorithms, and artificial intelligence have been utilized in some instances, as evidenced by a few examples in recent years [4–6]. In real terms, during the last twenty years, several investigations have been performed to

study the influence of icing on wind turbines using simulation methods. These studies aim to enhance our understanding of the phenomenon and provide valuable insights for designing more resilient and efficient wind turbine systems [7–10].

Computational fluid dynamics (CFD) is a common tool used to simulate various phenomena in turbomachinery [11], including the accumulation of ice on specific blade sections of the wind turbine [12]. The amount of ice accretion is predicted by numerical models, which can affect the airfoil geometry and decrease aerodynamic performance. Some examples of such studies include Etemaddar et al. [13]; Villalpando et al. [14]; Han, Kim and Kim [2]; Jin and Virk [15,16]; Yirtici et al. [17], Yirtici et al. [18].

In most computational fluid dynamics (CFD) studies focused on icing events in wind turbines, the flow along the blade span is often neglected due to its complexity and high computational costs. Instead, these studies usually focus on two-dimensional airfoil profiles placed at specific sections of the blade span. The decision to simplify the analysis using 2D airfoil models and neglecting the 3D rotating effect is driven by practical considerations. Accounting for the full 3D rotational flow requires significantly more computational resources and time. By focusing on specific sections of the blade span, researchers can still gain valuable insights into the aerodynamic behavior of the wind turbine under icing conditions while keeping the computational requirements within manageable limits. While this approach may introduce some limitations in capturing the complete 3D flow physics, it still provides valuable information for understanding the impact of ice accretion on the performance of wind turbines. Researchers continue to explore advancements in modeling techniques and computational capabilities to better address the complexities of 3D rotating flows in future studies [19–21].

After conducting a review of the literature, it was noticed that popular icing programs were initially designed for simulation icing in aeronautics [3,22–24]. The icing programs primarily developed for simulating aircraft icing are not specifically tailored to account for wind turbines' distinct operational and weather conditions. Wind turbines and aircraft exhibit distinct icing dynamics attributed to various factors. These factors encompass differences in operational altitude, angle of attack (AoA), airfoil positioning concerning the ground, the contrast between fixed-wing and rotating blades, and the impact of air compressibility at varying airspeeds [24].

Indeed, a few programs for in-flight icing have undergone adaptations, testing, and validation to replicate the formation of ice on the blades of wind turbines. The main emphasis of these adjustments lies in integrating the distinctive atmospheric conditions during operation and accounting for the geometry and rotation of the wind turbine blades. Consequently, models originally crafted for simulating icing on aircraft may display incongruent behaviors when employed in simulations for wind turbines. The distinctions in operational conditions and blade characteristics necessitate adjustments to the existing models. For instance, wind turbine blades experience different airspeeds, air temperatures, and humidity levels compared to aircraft wings. The rotation of wind turbine blades introduces a time-varying flow field, leading to variations in the ice accretion patterns.

Additionally, the complex geometry of wind turbine blades, including their twist and taper along the span, requires specific considerations for accurate simulation. By adapting, testing, and validating these in-flight icing programs for wind turbines, researchers and engineers aim to address these incompatibilities and develop models that effectively capture the icing behavior unique to wind turbines. These modifications enable more reliable assessments of ice accretion effects and aid in designing and optimizing wind turbine systems for safe and efficient operation in icy conditions [12,14,24]. For instance, Etemaddar et al. [13] concluded that wind turbines could operate under icy conditions by reducing their cut-off speed to minimize the risk of damage to components. The authors used LEWICE 1.6 software and the Blade Element Momentum (BEM) code WT-Perf to reach this conclusion. Another example is the study of Han, Kim and Kim [2], in which a CFD model was used to suggest that modifying the pitch angle is necessary for maintaining steady power in wind turbines during icing periods. However, the study concluded that

maximum turbine efficiency under these conditions can be achieved below the rated speed by operating at a variable speed via generator torque control.

While software packages like NASA's LEWICE and FENSAP-ICE (currently part of ANSYS) are commonly employed for investigating icing, they have predominantly been utilized in aeronautical applications. LEWICE and FENSAP-ICE have been extensively used and validated for simulating ice accretion on aircraft surfaces. These packages incorporate specialized algorithms and models tailored to aircraft icing phenomena, considering droplet impingement, ice shape evolution, and ice shedding. However, their application to wind turbine icing simulations requires careful evaluation and adaptation to account for wind turbines' unique characteristics and operational conditions.

To effectively utilize these software packages for wind turbine icing studies, validating their performance against experimental data and real-world observations specific to wind turbines is essential. This process involves assessing their ability to capture ice accretion patterns, evaluating the effects on aerodynamic performance, and accounting for the complex interactions between rotating blades, atmospheric conditions, and ice-shedding dynamics. By conducting thorough testing and validation, researchers and engineers can enhance the reliability and accuracy of these software packages for wind turbine icing simulations, enabling a better understanding and mitigation of icing-related challenges in the wind energy industry [19,25].

However, using these two programs, various investigations have devised approaches for replicating ice accumulation on wind turbine blades [15,26–28]. Homola et al. [29] employed FENSAP-ICE to anticipate the formation of ice on the airfoils of the NREL 5MW benchmark wind turbine. In the study of Etemaddar et al. [13], FLUENT was utilized for aerodynamic computations and ice accretion was simulated using LEWICE. The resultant lift and drag coefficients, C_L and C_D, were computed through ANSYS FLUENT and then corroborated against experimental measurements from the wind tunnel at "LM Wind Power".

The simulation of ice accretion usually comprises a sequence of four primary modules [24,30,31]. The first module involves aerodynamic calculations to determine the flow characteristics around the wind turbine blade. This is achieved by solving the Navier–Stokes equations, including continuity (Equation (1)), momentum (Equation (2)), and energy (Equation (3)).

$$\frac{\partial \rho_a}{\partial t} + \vec{\nabla} \cdot \left(\rho_a \vec{U} \right) = 0 \tag{1}$$

$$\frac{\partial \rho_a \vec{U}}{\partial t} + \vec{\nabla} \cdot \left(\rho_a \vec{U} \vec{U} \right) = \vec{\nabla} \cdot \sigma^{ij} + \rho_a \vec{g} \tag{2}$$

$$\frac{\partial (\rho_a E_a)}{\partial t} + \vec{\nabla} \cdot \left(\rho_a \vec{U} H_a \right) = \vec{\nabla} \cdot \left[k_a \left(\vec{\nabla} T_a \right) + U_i \tau^{ij} \right] + \rho_a \vec{g} \cdot \vec{U} \tag{3}$$

In this context ρ_a denotes air density and $\vec{U}$ represents the fluid velocity vector. The subscript a pertains to the air solution, T denotes the static air temperature measured in Kelvin, σ^{ij} signifies the stress tensor, k_a is the thermal conduction coefficient, and E and H are the total initial energy and enthalpy, respectively. Usually, such equations are supplemented with turbulence models aimed at describing the fluctuating characteristics of the flow around the wind turbine blades.

The second module focuses on calculating the trajectory of water droplets in the airflow. This can be performed using either a Lagrangian approach, which tracks individual droplets, or an Eulerian approach, which considers the behavior of droplets as a continuous phase. Simulating the droplet trajectories, the module determines where the droplets impinge on the blade surface. The third module entails thermodynamic computations to evaluate the rate of ice accumulation in a specific location over a designated period. These calculations consider air temperature, humidity, and droplet properties to estimate how ice accumulates on the wind turbine blade surface. The fourth module deals with

the geometry of the wind turbine blade and enables updating the blade shape as the ice grows. This is important because ice accretion alters the blade's geometry and surface roughness, affecting its aerodynamic performance. The module ensures that the evolving geometry due to ice growth is accurately represented in the simulation. By integrating these four modules into a comprehensive simulation framework, researchers and engineers can obtain insights into the aerodynamic effects of ice accretion on wind turbine blades and make informed decisions regarding turbine design, operation, and ice protection strategies.

This layer of ice enhances the likelihood of boundary layer detachment on the suction side of the airfoil, known as the extrados, resulting in an aerodynamic stall occurring at a lower AoA compared to a clean scenario without ice. Given the intricate nature of this phenomenon, the fluctuations in flow velocity and the formation of eddies become exceedingly challenging to predict. Addressing these disturbances at a small scale necessitates employing an unsteady Navier–Stokes equation and incorporating a high level of detail. However, these vortices and fluctuations diminish in size at higher Reynolds numbers. Hence, the Reynolds averaged Navier–Stokes (RANS) approach becomes more appropriate where the velocity fluctuations in the flow field are averaged over time [24].

Various Reynolds-averaged Navier–Stokes (RANS) models and adaptations are accessible, contingent upon the specific application, each relying on distinct methodologies for computing turbulent eddy viscosity. Addressing this diversity, numerous turbulence models, including but not limited to Spalart–Allmaras, k-epsilon, k-omega, shear-stress transport (k-omega SST model), and large eddy simulation (LES), are usually employed. These models are extensively applied in studying flows surrounding airfoils and wind turbines [24].

The Spalart–Allmaras model (SA) is a one-equation turbulence model. This additional equation models the turbulent viscosity transport. This model is employed in aerodynamics because of its compromise between computational cost and accuracy [24]. The k-epsilon model stands as a turbulence model with two equations, addressing both the turbulent kinetic energy (k) and the rate at which it dissipates (epsilon). It has demonstrated adequate performance in simulating ice accretion, gaining widespread popularity owing to its numerical stability, efficiency in computational resources, and rapid convergence rate [24,29,32]. The k-omega model is also a two-equation model that solves the turbulent kinetic energy (k) and the specific dissipation rate of kinetic energy (omega). It is used in cases where k-epsilon is insufficient but has a lower convergence rate as it is more non-linear [33]. Finally, the k-omega SST model, introduced by Menter [34], represents a two-equation model that amalgamates features from the k-omega and k-epsilon models. It employs these models in distinct flow regions, activating the k-omega model close to the wall and resorting to the k-epsilon model when situated away from the surface [24]. Such a turbulence model is more accurate than others because of its ability to handle flow recirculation zones, offering a satisfactory approximation of flow separation and elucidating the creation of distinct vortices at both the trailing and leading edges [24,34,35].

Reference [24] addressed the various modeling approaches and simulation techniques available for wind turbine icing. This article specifically highlighted the distinct characteristics of wind turbine icing simulations, including the unique operational conditions and software capabilities required. Furthermore, the potential and suitability of various software tools for wind turbine icing simulations were thoroughly discussed. In particular, the adaptability of software FENSAP-ICE for wind turbine icing simulations, its integration with ANSYS, and the insights provided by the previously published articles collectively contribute to the growing understanding and progress in the modeling and simulating of icing on wind turbines. These developments facilitate more accurate assessments of the impact of icing on wind turbine performance and aid in designing mitigation strategies to ensure safe and efficient wind turbine operations.

Recently, Martini, Ibrahim, Contreras M, Rizk and Ilinca [12] performed a computational analysis on a NACA 64-618 airfoil of the iced NREL 5MW benchmark wind turbine, utilizing ANSYS FLUENT and FENSAP-ICE. The investigation focused on evalu-

ating the precision of aerodynamic loss estimation for airfoils affected by icing using two turbulence models (Spalart–Allmaras and k-ω SST) and the effect of surface roughness distribution using the Shin et al. [36] model available in the ICE3D module in FENSAP-ICE. Etemaddar et al. [13] and Homola et al. [29] used published research, numerical investigations and experimental studies in the existing literature for comparison. These authors found that neglecting surface roughness from calculations underestimates the effect of ice on aerodynamic performance. On the other hand, they concluded that the choice of turbulence model had a limited influence on the resulting aerodynamic losses caused by icing, compared to the impact of considering roughness. A similar conclusion was attained by the authors of [37], where they found that the extent of the ice-induced roughness and its height drove the decrease in the aerodynamic performance of the studied airfoils as the angle of attack increased.

The previous discussion demonstrates that the accuracy of icing modeling depends heavily on roughness, which has been emphasized by various authors in the field [24,38–40]. Roughness plays a significant role in airfoil performance as it affects the boundary layer transition and flow separation, critical factors in aerodynamic efficiency [39–41]. Even small amounts of ice can significantly affect an airfoil's performance. Therefore, it is crucial to consider the effects of roughness at every step of the ice growth calculation [37,41]. Considering the roughness height as a parameter in heat transfer analysis ensures that the effects of surface roughness on convective heat transfer are adequately accounted for, leading to more reliable and precise thermal assessments and design considerations [42,43]. For example, modelers studying aircraft icing extensively utilized computational fluid dynamics (CFD) to analyze the local heat transfer coefficient across various aircraft components. The findings suggested that surface roughness could substantially amplify local heat transmission, even in the presence of a thin layer of ice [44].

However, determining the roughness height of structures such as wind turbine blades necessitates conducting experiments, as detailed in the study of Blasco, Palacios and Schmitz [40]. These experiments can be tedious and costly, and their applicability is limited as they depend on the airfoil type and wind tunnel configuration. In response to the above, different research centers have various ways of describing roughness [24]. For instance, the traditional NACA roughness model originated through distributing typical grain sizes uniformly from the leading edge downstream on both the pressure and suction surfaces [45]. The sand-grain roughness model of Shin et al. [36], initially designed for aeronautics, is the most frequently employed correlation for predicting ice surface roughness along wind turbine blades. This model was specifically designed to match the ice shapes predicted by the LEWICE code to experimental ones and for the atmospheric conditions typical of aviation, which makes the model lack generality [37]. This empirical correlation relies on the Shin and Bond formula, which computes the non-dimensional height of small-scale surface roughness: k_s/c as a function of static temperature, airfoil chord length c, median volume diameter (MVD), liquid water content (LWC), and the relative wind speed (see Equation (4)).

$$k_s = 0.6839 \left[\frac{k_s/c}{(k_s/c)_{base}}\right]_{LWC} \cdot \left[\frac{k_s/c}{(k_s/c)_{base}}\right]_{T} \cdot \left[\frac{k_s/c}{(k_s/c)_{base}}\right]_{MVD} \cdot \left(\frac{k_s}{c}\right)_{base} \cdot c \quad (4)$$

where each sand-grain roughness parameter is provided by Shin et al. [36]:

$$\left[\frac{k_s/c}{(k_s/c)_{base}}\right]_{LWC} = 0.5714 + 0.2457(LWC) + 1.2571(LWC)^2 \text{ for LWC } > 1 \text{ g/m}^3 \quad (5)$$

$$\left[\frac{k_s/c}{(k_s/c)_{base}}\right]_{T} = 0.047(T) - 11.27 \quad (6)$$

$$\left(\frac{k_s}{c}\right)_{base} = 0.001177 \quad (7)$$

$$\left[\frac{k_s/c}{(k_s/c)_{base}}\right]_{MVD} = \begin{cases} 1 & MVD \leq 20 \\ 1.667 - 0.0333(MVD) & MVD > 20 \end{cases} \quad (8)$$

An alternative to the previous roughness model is the so-called beading model available in ANSYS-FENSAP-ICE. This model considers both constant and varying distributions of sand-grain roughness and integrates them into the existing turbulence models. After activation of the beading model, the prediction of sand-grain roughness height on the surface caused by moving and freezing beds is enabled [38], i.e., there is an automatic transfer of the spatially and temporally evolving roughness data to the airflow module at the end of each shot. As a result, the roughness height changes dynamically and depends on the contaminated area.

As a matter of fact, the sand-grain roughness model of Shin et al. [36] is used in nearly every CFD investigation focused on icing, where it is employed to gauge the roughness of the ice-covered surfaces on wind turbine blades [24,37]. However, as far as we know, there is a scarcity of icing studies in the literature comparing the influence of the surface roughness model, particularly the beading model, on the aerodynamic performance of wind turbine airfoils.

Therefore, this paper presents a numerical study conducted in the iced S809 airfoil where the impact of the surface roughness model on its aerodynamic coefficients is addressed. Moreover, the influence of the employed turbulence model is also evaluated. The results for the clean airfoil were validated with the experiments in [46] and simulations of [47]. The predicted rime ice shape was validated with the experimental studies of [48]. Two methodologies for estimating roughness (the Shin et al. [36] model and beading model) are compared, as well as the effect of icing type, rime ice, and the much less studied case of glaze ice on aerodynamic performance. Such influence of icing conditions and roughness is evaluated and discussed by examining the lift and drag coefficients and skin friction and pressure coefficients.

2. Geometrical Configuration and Mesh Generation

The geometrical model was based on an airfoil used by the National Renewable Energy Laboratory (NREL). The S809 airfoil is used in the two-bladed NREL Phase VI turbine [49], which is present along the entire length of the blade. This study will focus on the section at 95% radius of the blade, primarily because it corresponds to the area closest to the blade tip, where ice accumulation is most prevalent. Furthermore, this region of the blade is the main region responsible for turbine performance [50,51]. The chord of the S809 at this radius is 0.358 m, and the airfoil has the following specifications [52]:

Max thickness: 21% at 39.5% of the chord from the leading edge.

Max camber: 1% at 82.3% of the chord from the leading edge.

The geometric model was constructed using the DesignModeler 2022 R1 software, which is part of the ANSYS suite. Figure 1 illustrates the model, showcasing a sizable computational domain encompassing crucial flow disturbances, particularly downstream. The positioning of boundaries and the size of the domain were determined based on prior studies that demonstrated satisfactory agreement with experimental and numerical data. For example, the computational domain used by Villalpando, Reggio and Ilinca [14] and Hildebrandt and Sun [39] was extended by 12.5 chords in front of the airfoil and 20 chords behind; in the case of Zanon et al. [53], the domain boundaries were located at 20 chord lengths. Considering the above, the chosen dimensions of the computational domain were the same as the ones used by [53]. This guarantees that the boundary conditions applied to the external domain do not disrupt the flow in the neighboring region or compromise the accuracy of the results.

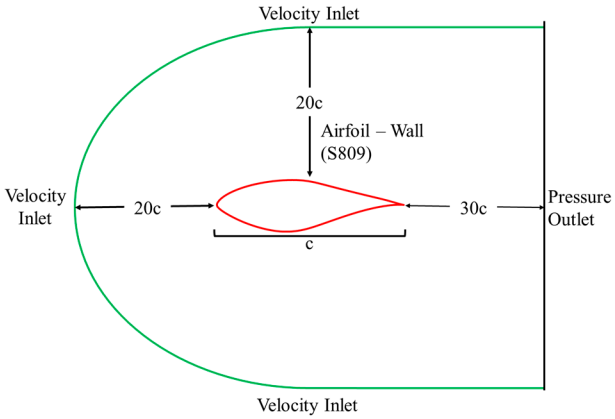

Figure 1. Illustration of the computational domain geometry.

The computational domains have been discretized using a non-structured grid generated with ANSYS Meshing 2022 R1 software. Figure 2 provides an overview of the utilized meshes. To adequately describe the boundary layer development, the mesh around the airfoil has an O-grid topology, including 25 prism layers (see Figure 3). Beyond the prisms zone, a non-structured mesh based on tetrahedra was created, ensuring their aspect ratio is close to the prisms to guarantee a smooth transition between both mesh regions.

The following sections present the calculations for ice accretion, including an estimation of the aerodynamic characteristics of clean and iced airfoils. Additionally, the performance losses occurring under specific icing scenarios are evaluated.

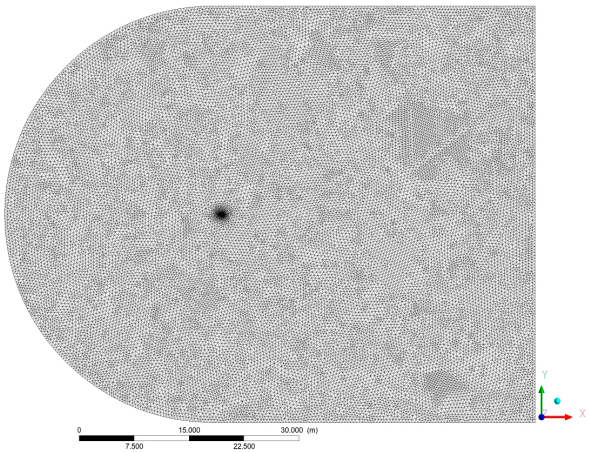

Figure 2. Overview of the mesh in the computational domain.

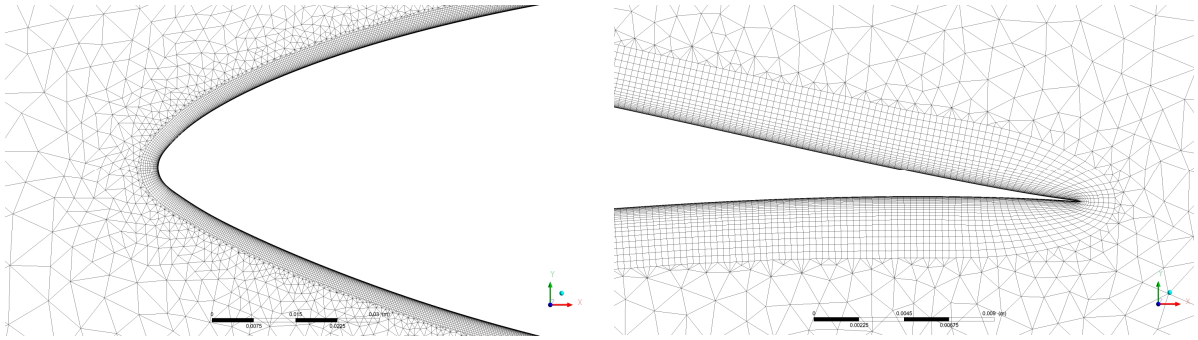

(**a**) (**b**)

Figure 3. Detail of the prism layers around the airfoil. (**a**) Leading edge. (**b**) Trailing edge.

3. Numerical Simulation Setup and Verification Study

Simulations of ice accretion on the S089 airfoil were carried out with the software FENSAP-ICE integrated into the ANSYS platform. They were performed on a desktop computer with a Windows 11 operating system, Intel Core i5 10th generation processor @ 2.90 GHz, and 24 GB RAM.

FENSAP-ICE operates in a modular system (see Figure 4) with three components: the FENSAP module is used for aerodynamic calculations, DROP3D is used for droplet impingement, and ICE3D is used for ice growth calculations. Moreover, FENSAP-ICE has two methods to estimate the roughness due to ice accretion: the beading model and the Shin et al. [36] model; both methods were used to compare their effect on the airfoil aerodynamic coefficients. Data regarding the simulation setup can be found in Table 1 for two ice conditions: rime (dry regime) and glaze (wet regime).

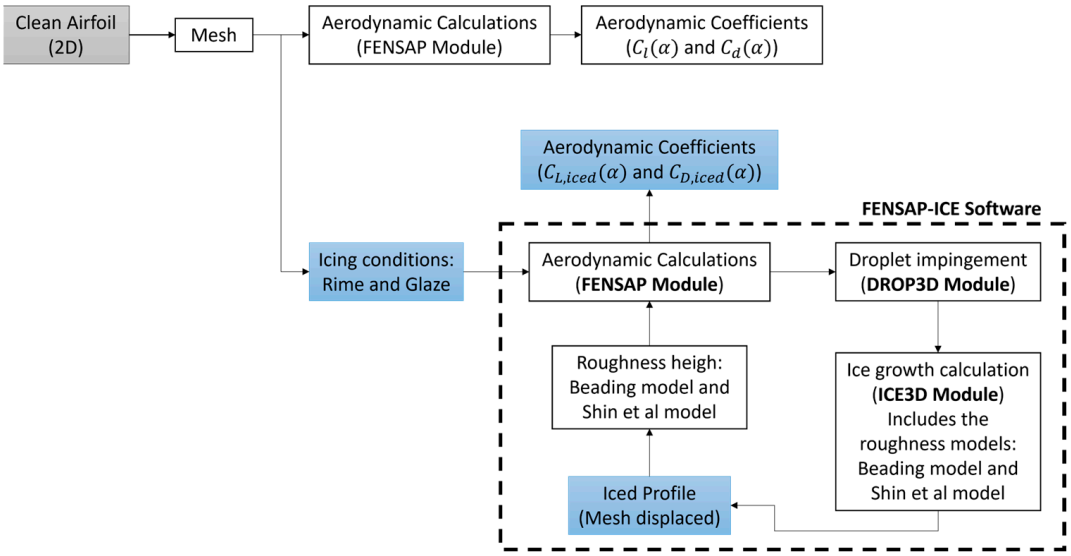

Figure 4. Flowchart of the CFD simulation using FENSAP-ICE.

Table 1. Overview of the simulation parameters.

Parameters	Rime	Glaze
Air speed U [m/s]	42	42
Angle of attack, AoA [°]	4	4
Reynolds number	3.4×10^6	3.4×10^6
MVD [μm]	20	27
LWC [g/m^3]	0.05	0.12
Ice density [kg/m^3]	750	917
Accretion time (min)	30	30
Temperature (°C)	−10	−5
Turbulence model	Spalart–Allmaras/k-ω SST	Spalart–Allmaras/k-ω SST
Convergence criterion	1×10^{-5}	1×10^{-5}

Note: the parameters for the rime condition were taken from Han, Palacios and Schmitz [48] to validate and compare the results. The glaze ice condition parameters were estimated based on in situ measurements from the non-profit applied research center "Nergica" in Québec, Canada.

The validation of the flow around the clean airfoil was performed with the two considered turbulence models under the same conditions described in Table 1. The Spalart–Allmaras (SA) model was chosen because it is widely used in aerodynamics and due to its good computational cost/accuracy performance ratio and the k-ω SST model was chosen because it is more robust and performs better in flows with strong adverse pressure gradients.

A spatial verification test or mesh independence study was performed in the no-ice conditions. Three distinct grids were created to verify mesh convergence, adjusting the number of elements. Localized mesh refinement was opted for, indicating that variations in spatial discretization are concentrated around the airfoil. The procedure commenced with a coarse discretization at the outer limit of the boundary layer and progressed to a finer discretization along the profile wall (see Table 2).

Table 2. Number of elements in the considered meshes.

Mesh	Number of Elements
1	870,726
2	1,235,620
3	1,655,379

Intending to resolve the boundary layer development, all the grids use a thin layer around the airfoil, which is discretized by 25 layers of prisms. The initial height of these layers was set at 7.6×10^{-6} m, a value determined to maintain $y^+ < 2$. This value of the variable y^+ is suggested by the numerical requirements imposed by the k-ω SST turbulence model.

The CFD grid independency study involved calculations in successively refined meshes, evaluating the convergence of the most relevant variables. The lift and drag coefficients, C_L and C_D, were chosen in this case. They are defined as:

$$C_L = \frac{L}{\frac{1}{2}\rho c U^2}; \; C_D = \frac{D}{\frac{1}{2}\rho c U^2} \tag{9}$$

where L and D represent the dimensional lift and drag forces, and c is the airfoil chord length.

Table 3 showcases the verification outcomes for the generated meshes. The convergence error, expressed as a percentage, was computed by assessing the difference in the aerodynamic coefficient for each mesh compared to the most refined mesh, i.e., mesh no. 3.

Table 3. Convergence errors for each mesh.

	K-ω SST Model				Spalart–Allmaras Model			
Mesh No.	**C_L**	**C_L Error**	**C_D**	**C_D Error**	**C_L**	**C_L Error**	**C_D**	**C_D Error**
1	0.5405	1.66%	0.014877	5.81%	0.5617	3.81%	0.013611	3.55%
2	0.5506	0.18%	0.015824	0.19%	0.5459	0.89%	0.014540	2.84%
3	0.5496		0.015794		0.5411		0.014058	

As can be seen in Table 3, the maximum difference between mesh no. 2 and 3 is less than 3%. Either mesh could be used for the study, so the computational cost was also used to decide. Although mesh no. 3 has 33% more elements, the difference in computational time was minimal, so it was decided to work with it. For example, the complete simulation (i.e., of the three modules FENSAP, DROP3D, and ICE3D) took 24 h for mesh #2 and 26 h for mesh no. 3. The convergence study was performed with the two turbulence models, the k-ω SST being the one with the lowest error percentage. In addition, as depicted in Figure 5, the lift and drag coefficients attain a nearly constant value, demonstrating that the achieved solution is mesh-independent.

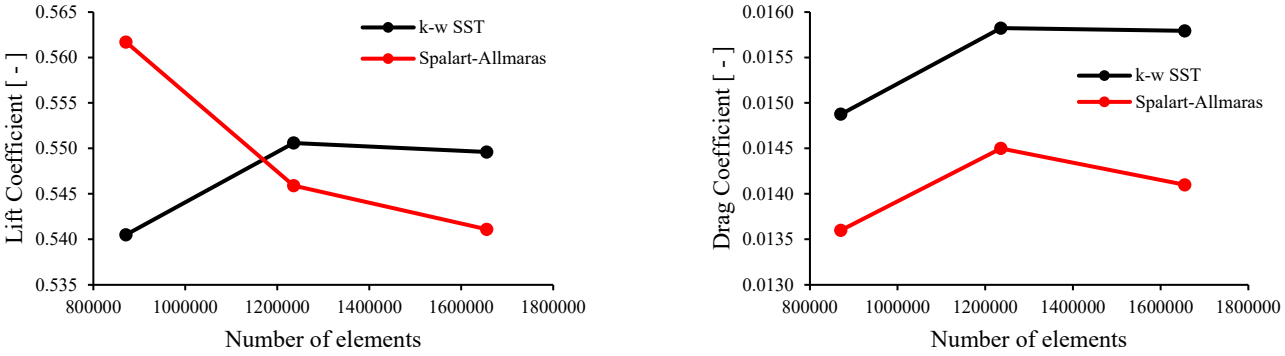

Figure 5. Aerodynamic coefficients vs. the number of elements. Lift coefficient (**left**) and drag coefficient (**right**).

As previously mentioned, FENSAP-ICE has three modules: FENSAP, DROP3D, and ICE3D; for each of them, the values of the relevant variables are given in Table 4.

Table 4. Parameter values in each ANSYS FENSAP-ICE module.

Parameters	FENSAP	DROP3D	ICE3D
Characteristic length		0.358 m	
Airspeed U		42 m/s	
Air static pressure		101325 Pa	
Air static temperature		−10 °C (rime) −5 °C (glaze)	
Velocity angle of attack		4°	
Liquid water content (LWC)	n. a	0.05 g/m^3 (rime) 0.12 g/m^3 (glaze)	0.05 g/m^3 (rime) 0.12 g/m^3 (glaze)
Droplet diameter (MVD)	n. a	20 µm (rime) 27 µm (glaze)	n. a
Droplet distribution	n. a	Monodisperse	n. a
Total time of ice accretion		n. a	1800 s
Roughness model		n. a	Beading model/ Shin et al. [36] model

Upon completing the simulation, ICE3D produced the geometry of the iced airfoil, generating the computational mesh, which was subsequently employed to estimate aerodynamic lift and drag coefficients under rime and glaze ice conditions.

4. Results and Discussion

The results presented here demonstrate the validation of the obtained aerodynamic parameters for the S809, comparing them with experimental data and findings from prior numerical studies on this airfoil [46–48]. The performed CFD simulations consider two turbulence models in conjunction with two roughness scenarios and two different types of icing (rime and glaze).

In computational fluid dynamics (CFD) simulations, several models are used to account for turbulence development, including the models chosen in this work: Spalart–Allmaras (SA) and k-ω SST, which belong to the Reynolds-averaged Navier–Stokes (RANS) family. These models have been widely studied in the literature for wind turbines [35]. The k-ω SST model is advantageous for modeling flows around wind turbine blades as it allows analyzing the turbulent boundary layer at large angles of attack [54]. On the other hand, the Spalart–Allmaras model is often used due to its low computational cost and acceptable precision in turbulent flow modeling, particularly in aerospace applications [29,55]. However, it has a disadvantage in describing the boundary layer behavior with adverse pressure gradients compared to the k-ω SST model [12].

4.1. Clean Airfoil

Clean airfoil drag and lift coefficients were estimated to assess the aerodynamic loss due to icing. Then, the results were compared with the measured coefficients on the same airfoil under varying angles of attack, serving as a validation for the simulation. The CFD simulation results of the S809 airfoil were validated with experimental data from Somers [46]. The numerical flow coefficients were also compared with the CFD study by Tan [47], using the same turbulence model (Spalart–Allmaras).

The experimental study carried out by Somers [46] took place at the low-turbulence wind tunnel of the Delft University of Technology Low-Speed Laboratory in the Netherlands. The study's primary objectives were to achieve a maximum lift coefficient insensitive to roughness and obtain low-profile drag coefficients within a specific range of lift coefficients and Reynolds numbers. The airfoil model used in the experimental study was made of aluminum, with a chord length of 600 mm and a span of 1248 mm. The model was tested at various Reynolds numbers based on the airfoil chord, ranging from 1.0×10^6 to 3.0×10^6. The tests were conducted with the airfoil surface both smooth (without roughness) and with roughness introduced at specific locations (0.02c on the upper surface and 0.05c on the lower surface) to promote the transition of the boundary layer from laminar to turbulent.

Regarding Reynolds number effects, at the design Reynolds number (2.0×10^6), the maximum lift coefficient achieved was approximately 1.01, which met the design objective of 1.0 [46]. The trailing-edge stall behavior was gentle and occurred at approximately 20° angle of attack. Minimal hysteresis was observed at angles of attack beyond the maximum lift and below the minimum lift. Concerning the effect of roughness, Somers [46] found that the maximum lift coefficient was not significantly affected by the addition of roughness at any of the Reynolds numbers tested. However, when using fixed transition, the drag coefficients tended to be excessively high at both low and high lift coefficients. This fact was primarily attributed to the roughness height being comparable to the boundary-layer thickness on the upper surface at low lift coefficients and on the lower surface at high lift coefficients. This resulted in an additional contribution to drag known as pressure drag, caused by the roughness itself. The impact of roughness on drag was more pronounced at higher Reynolds number.

The simulations by Tan [47] assessed the aerodynamic performance of the NREL S809 airfoil with a trailing-edge flap. The length of the airfoil chord was 1 m, and a structured mesh of 150,000 cells around the airfoil was used. The simulations were performed using the commercial CFD software ANSYS Fluent 2022 R1 to solve the RANS equations in conjunction with three turbulence models (Spalart–Allmaras, SST k-ω, and Wray–Agarwal) at Reynolds number 10^6 (free stream velocity equal to 15 m/s) at angles of attack from 0° to 20°. The computations were performed with double precision, with a second-order upwind scheme for the convection terms and a second-order central difference scheme for the diffusion terms, and the SIMPLE algorithm was used for the pressure-velocity coupling. Only the results of the unmodified profile with the Spalart–Allmaras turbulence model were used to validate this study.

As shown in Figure 6, the lift coefficients estimated with the two turbulence models are close to those obtained experimentally by [46]; however, at an AoA of 15°, the CFD results slightly overpredict the experimental values. The disagreement between computations and experimental data at this AoA can be explained by the stall experienced by the airfoil, which is a phenomenon difficult to compute.

In the case of the drag coefficient (see Figure 7), both turbulence models presented a slight overestimation for angles of attack of 0° and 5° and an underestimation for angles of attack of 10° and 15°. This behavior is similar to that found by [12] and is associated with the stall phenomenon. The difference between the present SA computations and those of [47] are only significant at an AoA of 15°, and they are attributed to the known drawbacks of the SA turbulence model in regions characterized by high-pressure gradients [1]. Nevertheless, the disparity noted at elevated angles of attack between the experimental

data and numerical drag outcomes for the no-iced airfoil was deemed less critical because it appears beyond the operational ranges of the considered wind turbine [9,49].

Figures 8 and 9 depict the streamlines around the S809 airfoil, showing the flow recirculation zone (enclosed in the red circle) at an angle of attack of 15° for both turbulence models; the presence of such zones generates a decrease in lift and an increase in drag in the airfoil. The maximum error obtained with the k-ω SST model in C_L was below 10%, while the same error obtained with the Spalart–Allmaras model was 15%. This shows that the k-ω SST model better estimates the lift coefficient. On the other hand, when comparing the present C_L curve obtained with SA turbulence model with the results of [47], a maximum difference of 6% is observed even though the same turbulence model was used; this may be associated with the fact that this author used a much coarser structured mesh and the ANSYS Fluent software.

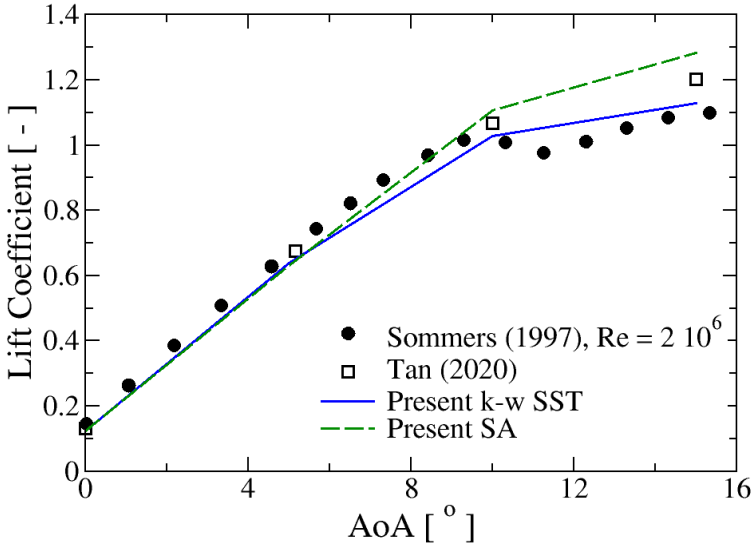

Figure 6. Lift coefficient versus AoA for the S809 airfoil, Sommers's data from [46], Tan's data from [47].

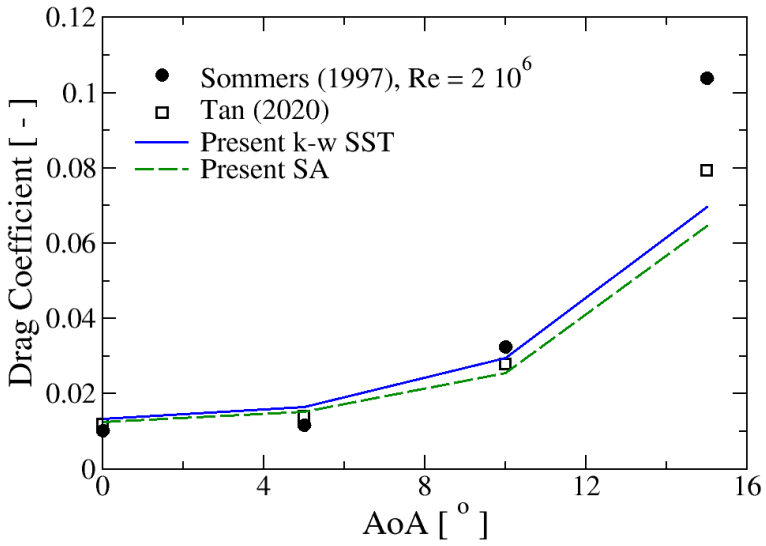

Figure 7. Drag coefficient versus AoA for the S809 airfoil, Sommers's data from [46], Tan's data from [47].

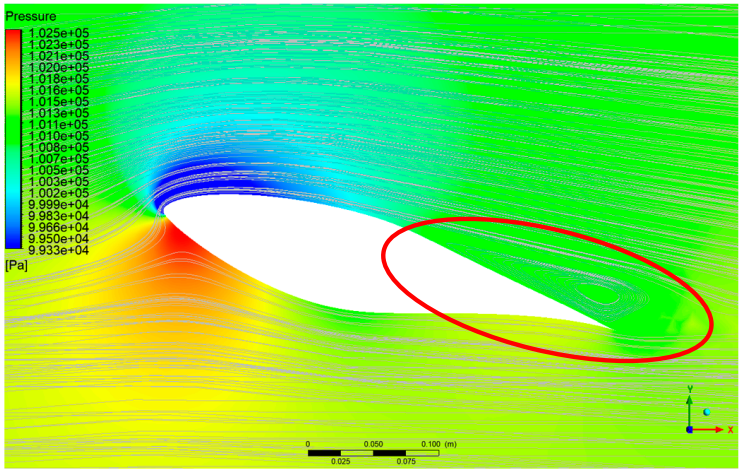

Figure 8. Pressure contours and streamlines at AoA of 15° of the clean profile using Spalart–Allmaras turbulence model.

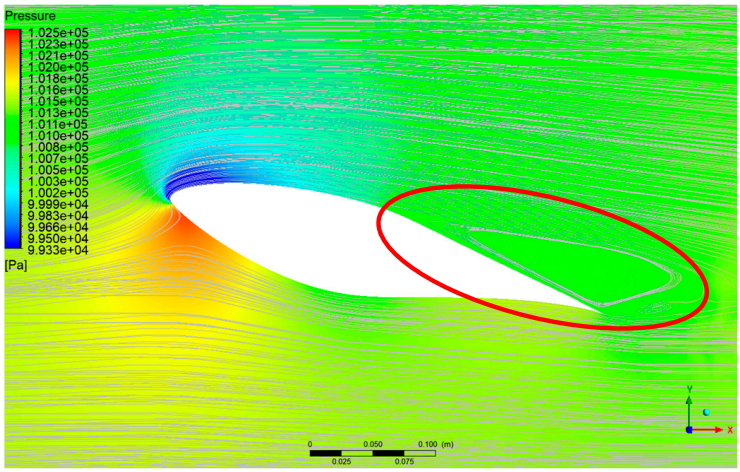

Figure 9. Pressure contours and streamlines at AoA of 15° of the clean profile using k-ω SST turbulence model.

Comparing the outcomes of both turbulence models, the lift coefficient estimate obtained with the Spalart–Allmaras model was approximately 5% higher on average than that obtained with k-ω SST. Consistently, the drag coefficient for the Spalart–Allmaras estimate was about 10% lower than the estimate obtained with the k-ω SST model.

Further insights about the flow behavior around the airfoil under separated conditions can be devised by analyzing the skin friction, C_f, and pressure, C_p, coefficients. They are defined as:

$$C_f = \frac{\tau_w}{\frac{1}{2}\rho U^2}; \quad C_p = \frac{p_g}{\frac{1}{2}\rho U^2} \tag{10}$$

$$\tau_w = \rho u^{*2} \tag{11}$$

where τ_w is the wall shear stress and p_g is the local gauge pressure.

Figure 10 shows the skin friction coefficient, C_f at AoA of 15°. The trends of both turbulence models are very similar, showing overlapping curves along the intrados (pressure side) and small differences in the extrados (suction side). In the figure, the stagnation and separation points can be identified as those with $C_f = 0$; the first ones are located close to the leading edge, while the second ones are approximately placed at half of the chord. It is seen that the Spalart–Allmaras model predicts a later boundary layer separation than the k-ω SST model, which is consistent with the streamlines depicted in Figures 8 and 9.

Figure 11 displays the pressure coefficients C_p also at an AoA of 15°. The upper side curves correspond to the suction side (extrados) and those of the lower side to the pressure side (intrados). Both turbulence models predict very similar values of C_p in the intrados but the SA model provides more negative pressure coefficients than the k-ω SST model along the first half of the chord in the extrados. The two models provide similar values in the second half of the chord. The higher suction forecasted by the SA model reflects a higher lift coefficient than that obtained with the k-ω SST model, as confirmed in Figure 6; consequently, the SA also yields a lower drag coefficient than the two-equation model.

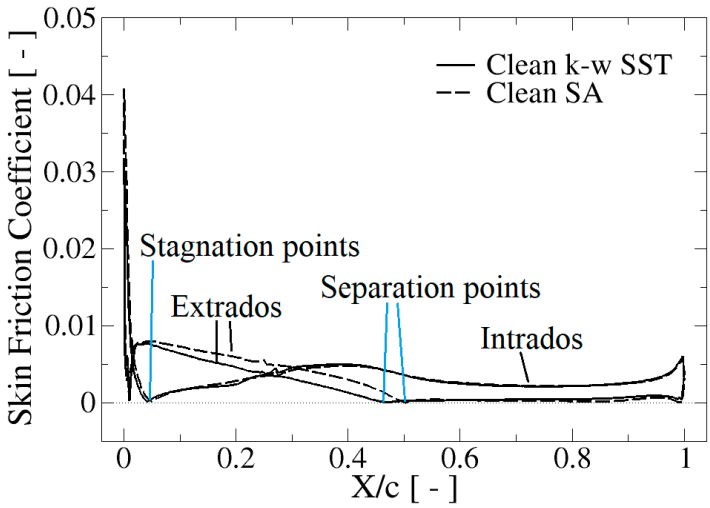

Figure 10. Skin friction coefficient at AoA of 15° of the clean profile with both turbulence models.

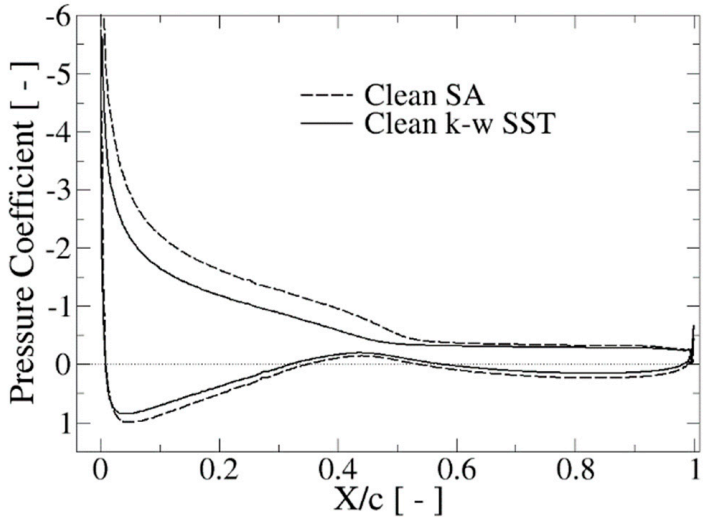

Figure 11. Pressure coefficient at AoA of 15° of the clean profile with both turbulence models.

In the subsequent analysis, considering that the likelihood of flow separation is increased by icing, the performance of both turbulence models in the presence of rime and glaze ice was investigated by comparing their results with those of the clean airfoil. Moreover, the effect of the roughness modeling on the aerodynamic coefficients is also studied.

4.2. Iced Airfoil

In Figure 12, the accumulation of ice at the leading edge is illustrated. A minor portion of the collected supercooled water does not instantly freeze upon contact with the airfoil's leading edge, leading the water to subsequently flow back and freeze at the

trailing edge beyond the impingement zone, a phenomenon observed in the study by Fortin and Perron [42].

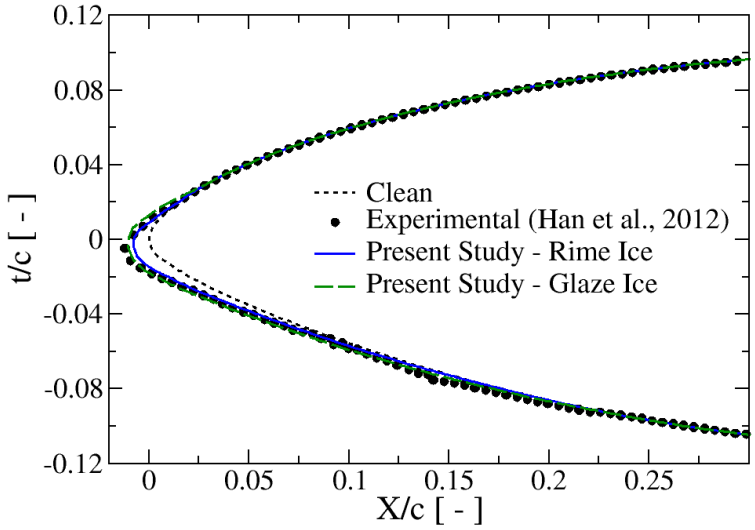

Figure 12. Comparison of the predicted ice shape (non-dimensional thickness versus non-dimensional chord) with the experimental results of Han et al. [48]. The clean shape, i.e., without ice, is also shown for comparison.

Concerning the leading edge (see Figure 12), the ice shape closely resembled the one depicted by Han et al. [48]. This similarity enables us to assert that the model and the simulation tools employed are adequate. However, the aerodynamic coefficients could not be validated because this study only showed the shape of the ice generated at the wind tunnel airfoil. However, since the alteration in the airfoil aerodynamic coefficients depends on the airfoil shape, it was decided that simulating a shape similar to that obtained experimentally would be sufficient. The validation was performed for both turbulence models.

It can be observed in Figure 12 that the ice shape for the two types of ice is quite similar, agreeing with [48], which is remarkable. Despite a 50% increase in LWC and a 35% increase in MVD in the case of the glaze ice, the difference in the accumulated ice shape at the leading edge is minimal and even comparable to the results obtained experimentally under rime ice conditions.

Since FENSAP-ICE performs the remeshing for the iced airfoil, it was decided to verify if the condition imposed for the y^+ was still satisfied. This parameter is essential since the performance of the k-ω SST model depends on its ability to describe the boundary layer development, so this value should be below 5 (or even less than 1) for better accuracy [56]. Although not shown, the values of y^+ for the clean airfoil are less than 1 throughout the profile, except for the leading-edge zone (30% of the profile), where it reaches a maximum value of 2.15. However, in the iced airfoil cases, the y^+ moderately increases, reaching a maximum value of 3.14, mainly at the airfoil's leading edge. This is to be expected since it is the area where the ice accumulates. Therefore, the corresponding elements experience a rearrangement or deformation.

Despite the increase in y^+, it can be stated that the remeshing process for the conditions studied is acceptable, and the meshes generated by the software satisfy the primary conditions for the turbulence model to provide accurate results. This, in turn, highlights the importance and attention that should be paid to the initial meshing process.

The results obtained for each simulated ice regime (dry and wet) are presented below. For each case, the effect of the turbulence and roughness models on the aerodynamic coefficients of the iced airfoil was evaluated.

4.2.1. Dry Regime—Rime Ice

Rime ice forms when supercooled water droplets, which are liquid droplets at temperatures well below freezing, i.e., lower than −10 °C, come into contact with the cold surfaces of the turbine blades. These supercooled droplets freeze quickly upon contact, adhering to the blade surfaces. Following [45], rime ice formation is favored at low temperatures, low liquid water content, small mean volume diameter, and low air velocities.

Regarding the results for the lift coefficient (see Figure 13), the obtained C_L was slightly higher than in the case of the no-ice airfoil at an angle of attack of 5°, 1.04% with the Spalart–Allmaras model and less than 2% with the k-ω SST model. This fact happens at low angles of attack, and it has been observed previously [37,40,46], probably because the ice-induced roughness at this AoA has a positive effect of triggering the transition from laminar to turbulent boundary layer, which is less prone to separation than the laminar one. There is a noticeable increase in drag (Figure 14) at this incidence angle, promoted by both the ice shape and the induced roughness [42,45]. However, for larger angles of attack, C_L in the iced configurations is notably reduced, and C_D is largely increased regarding the clean case; in fact, drag augments faster with growing AoA. This is because apparent roughness causes the stall phenomenon to be anticipated up to an angle of around 10°, as indicated in Figure 13. The most significant differences in lift between the different models are observed at an AoA of 10°. This fact can be explained by the sudden expansion of the separation zone, the uncertainty of the transition position, and the inaccuracy of the turbulence and roughness models in predicting them.

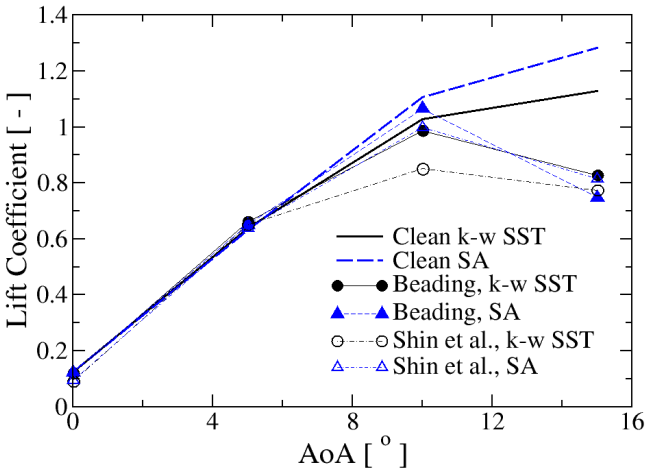

Figure 13. Lift coefficient for the rime ice, Shin's data from [36].

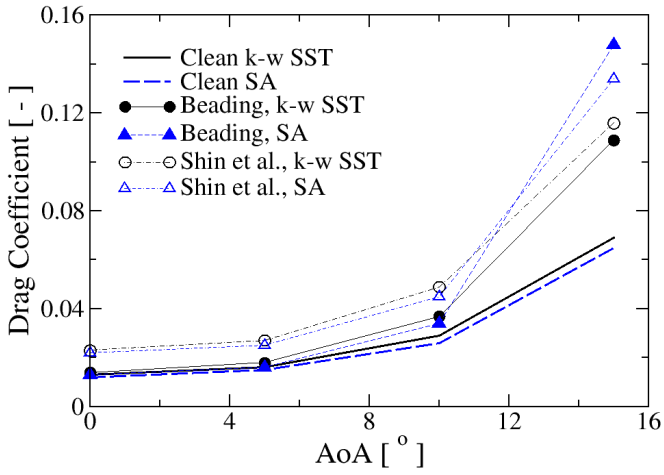

Figure 14. Drag coefficient for the rime ice, Shin's data from [36].

Interestingly, the Shin et al. [36] roughness model predicts a larger lift decrease than the beading model at high angles of attack. However, in the case of the SA turbulence model at 15°, such a trend is inverted, and the C_L provided by the beading model is lower than for the Shin et al. [36] model, a fact that does not happen for the k-ω SST formulation.

Figures 15 and 16 show the behavior of the skin friction (C_f) and pressure (C_p) coefficients in the iced configurations with rime ice at an AoA of 15°. Comparing with Figures 10 and 11, it can be seen that the peak of skin friction at the leading edge is higher in the case of ice than in the clean configuration; conversely, the maximum pressure coefficient magnitude at the same location is lower in the iced scenario than in the clean situation. Moreover, the overpressure in intrados is higher in the clean profile than in the case with ice; at the same time, in the first half of the chord, the suction is also higher than in the iced configuration. As a result, the lift coefficient decreases with the presence of ice. Regarding the friction coefficient, rime ice occurrence increases C_f in the intrados and promotes an earlier boundary layer detachment than in the clean profile. As a consequence, the separated flow region is the largest in the presence of rime ice, aggravating the stall phenomenon and implying lower lift and higher drag than in the no-ice configuration. Looking at Figures 15 and 16, the performance of both turbulence models in the iced scenario is very similar, showing some differences only in the location of the flow separation point in the extrados, which is predicted earlier by the SA than by the k-ω SST model.

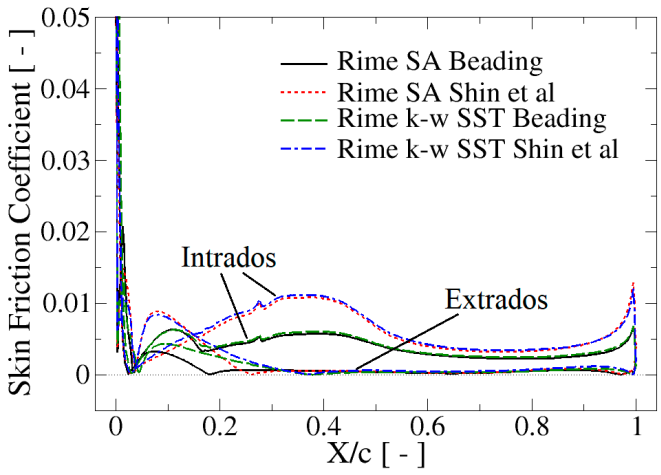

Figure 15. Rime ice: skin friction coefficient at an AoA of 15° of the iced profile with both turbulence and roughness models, Shin's data from [36].

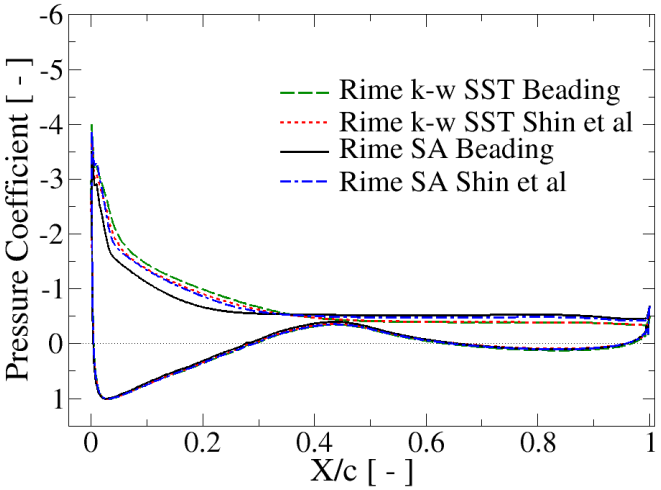

Figure 16. Rime ice: pressure coefficient at AoA of 15° of the clean profile with both turbulence and roughness models, Shin's data from [36].

Regarding the influence of the roughness model, it is found that its larger influence happens in the skin friction coefficient (Figure 15), showing only a moderate effect on C_p distribution along the leading half chord of the profile extrados (Figure 16). In the intrados, the Shin et al. [36] model predicts a noticeably higher C_f than the beading model, which is attributed to the extent of the rough region: the roughness height is uniform in the case of Shin et al. [36], while in the beading model, it is higher close to the leading edge, where the ice layer develops. Therefore, the larger the rough surface, the larger the wall shear stress, as should be expected. A similar situation happens in the extrados; logically, the friction coefficient is close to zero behind the point of flow separation. Here, the beading model predicts an earlier flow separation than in the Shin et al. [36] model, which implies a larger recirculation bubble on the extrados; this is illustrated in Figures 17 and 18 by the streamlines in the case of the SA turbulence model. Interestingly, in the intrados, the beading model predicts a secondary maximum of C_f close to the leading edge, around 10% of the chord length, precisely where the ice generates the higher roughness height. On the other hand, owing to the regular roughness distribution, the Shin et al. model displays a maximum much later, around 40% of the chord.

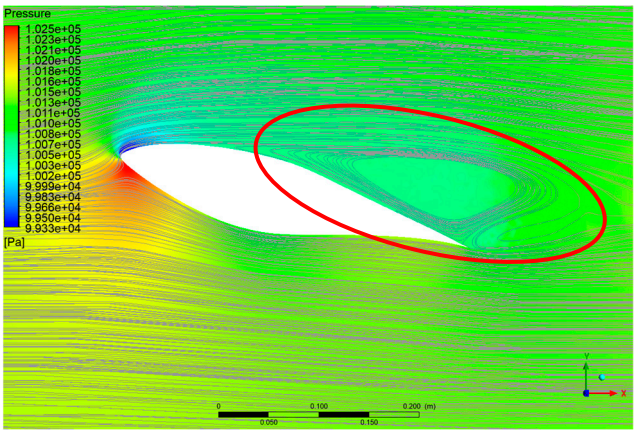

Figure 17. Rime ice: pressure contours and streamlines at AoA of 15°; beading model and Spalart–Allmaras model.

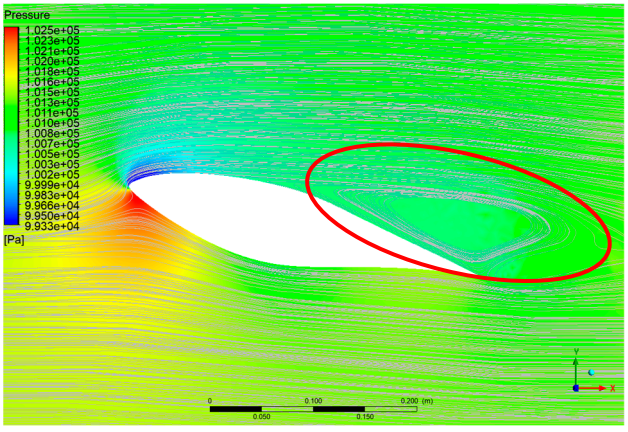

Figure 18. Rime ice: pressure contours and streamlines at AoA of 15°; Shin et al. [36] model and Spalart–Allmaras model.

As shown in Figure 19, the roughness estimated by the beading model and caused by ice affects mainly the airfoil leading edge (17% of the chord in this case). In comparison, the roughness estimated by Shin et al. is a fixed value along the 100% of the airfoil. This may imply an underestimation of the lift coefficient since the presence of roughness may accelerate the separation of the boundary layer. As can be seen from Figure 19,

the roughness estimated with the Spalart–Allmaras model is somewhat lower than that estimated by the k-ω SST model. From that figure, it can be seen that in the beading model, the ice roughness extends much more on the intrados than on the extrados.

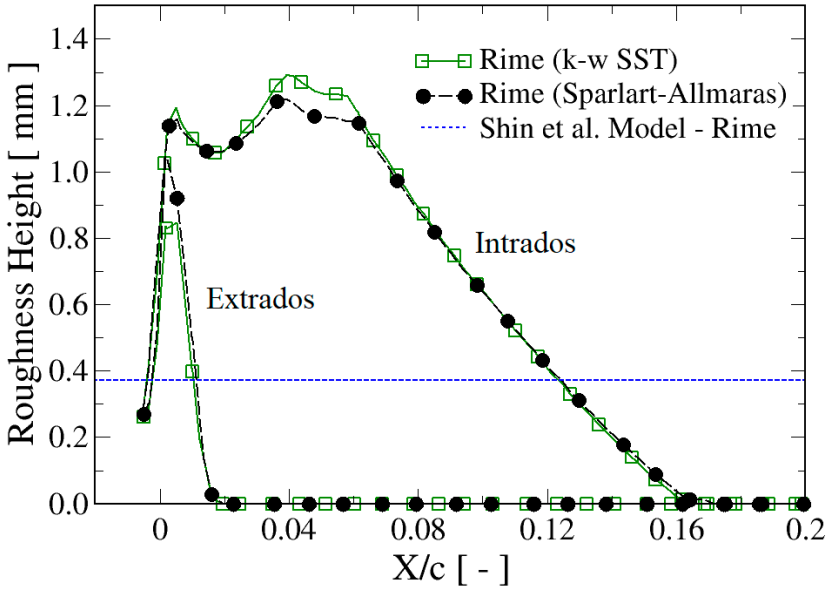

Figure 19. Distribution of the roughness height along the S809 airfoil for rime ice at an AoA of 15°, Shin's data from [36].

Using the beading model (see Table 5), it was found that for angles of attack of 0° and 10°, the loss in lift coefficient using both turbulence models was less than 5%. For an angle of attack of 5°, around a 3% increase in the lift coefficient was obtained with the two turbulence models. However, for 15°, there was a loss of 41.74% with the Spalart–Allmaras model and 26.78% with the k-ω SST model. The average loss in the lift coefficient was 9.10% using the k-ω SST model and 12.59% using the Spalart–Allmaras model. Regarding the drag coefficient, the behavior was as expected, and as the angle of attack increased, so did the drag coefficient, reaching its maximum at 15°. Again, the highest increase was estimated by the Spalart–Allmaras model, with an average value of 43.93%.

Table 5. Aerodynamic loss estimated using the beading model with rime ice.

	Clean				**Iced (Beading Model)**				**% Difference (Iced vs. Clean)**			
	Spalart–Allmaras		**k-ω SST**		**Spalart–Allmaras**		**k-ω SST**		**Spalart–Allmaras**		**k-ω SST**	
AOA (°)	C_L	C_D	C_L	C_D	C_L	C_D	C_L	C_D	C_L	C_D	C_L	C_D
0	0.124	0.012	0.123	0.013	0.124	0.013	0.120	0.014	−1.88%	6.73%	−2.16%	8.68%
5	0.632	0.015	0.639	0.016	0.651	0.016	0.662	0.018	3.13%	8.81%	3.43%	10.61%
10	1.106	0.026	1.029	0.029	1.066	0.034	0.988	0.037	−3.61%	31.67%	−4.04%	26.37%
15	1.284	0.065	1.129	0.069	0.748	0.148	0.827	0.109	−41.74%	128.51%	−26.78%	57.79%
				Average:					−12.59%	43.93%	−9.10%	25.86%

The Shin et al. model, shown in Table 6, predicts a more pronounced drop in C_L regarding the beading model: an average value of 17% for the SA model and around 19% for the k-ω SST model. However, the trend at an AoA of 5° is maintained with a forecasted slight increment of around 1% by both turbulence models. Likewise, a considerable augmentation in the drag coefficient is predicted by the Shin et al. [36] model, with mean increments of more than 80% and 68% for the SA and k-ω SST models, respectively.

Table 6. Aerodynamic loss estimated using the Shin et al. [36] model with rime ice.

	Clean				Iced (Shin et al. Model)				% Difference (Iced vs. Clean)			
	Spalart–Allmaras		k-ω SST		Spalart–Allmaras		k-ω SST		Spalart–Allmaras		k-ω SST	
AOA (°)	C_L	C_D	C_L	C_D	C_L	C_D	C_L	C_D	C_L	C_D	C_L	C_D
0	0.124	0.012	0.123	0.013	0.095	0.022	0.089	0.023	−22.96%	72.35%	−27.33%	72.70%
5	0.632	0.015	0.639	0.016	0.638	0.025	0.652	0.027	1.04%	66.96%	1.87%	68.00%
10	1.106	0.026	1.029	0.029	0.999	0.045	0.851	0.049	−9.61%	77.00%	−17.33%	65.94%
15	1.284	0.065	1.129	0.069	0.815	0.134	0.774	0.116	−36.50%	106.89%	−31.48%	66.70%
				Average:					−17.53%	80.80%	−19.50%	68.34%

Therefore, looking at the numbers in Tables 5 and 6, which are shown in Figures 13 and 14, it can be stated the Shin et al. [36] model tends to predict lower C_L and higher C_D in the iced airfoil than the beading model. This fact is attributed to the fact that the Shin et al. [36] model assumes that the entire profile is covered by ice. Therefore, the whole profile is considered to be a rough surface. On the contrary, the beading model assumes that the increase in roughness occurs only in areas contaminated by ice. In the case of the S809 profile, only the leading edge is contaminated (see Figures 12 and 19).

Additionally, looking at Figures 15 and 16, it can be concluded that the impact of turbulence modeling on the pressure and skin friction coefficients of the iced airfoil is lower than that of the roughness model.

4.2.2. Wet Regime—Glaze Ice

Glaze ice is formed in conditions of temperatures between −10 and 0 °C where the droplet, after impact, runs along the surface in the flow direction before freezing completely, occupying a wider surface than in the case of rime ice. The frozen liquid forms a smooth, transparent, and translucent layer of ice on the blade surface.

Regarding the results for the lift coefficient (see Figure 20), similarly to what happened for rime ice, the obtained C_L was a little bit over that of the clean airfoil at an angle of attack of 5°, between 2% and 3% depending on the turbulence and roughness models. However, for larger angles of attack, the lift coefficient decreases noticeably, even more than in the case of rime ice. Moreover, the drag coefficient increases at the same time, reaching higher values than in the case of rime ice (see Figure 21). Of course, this is again due to the anticipation of the stall phenomenon, which is illustrated by the streamline's behavior shown in Figures 22 and 23 in the case of the SA turbulence model and for the two considered roughness models.

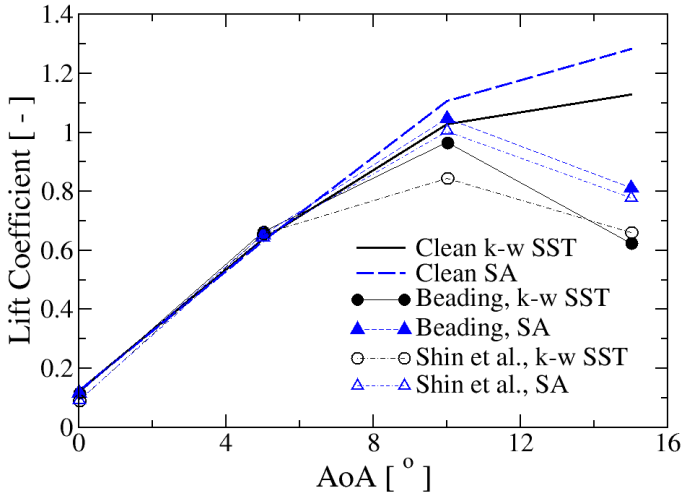

Figure 20. Lift coefficient for the glaze ice, Shin's data from [36].

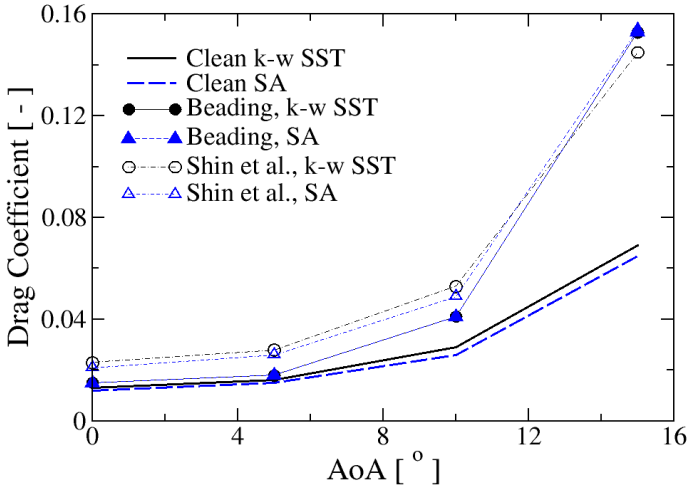

Figure 21. Drag coefficient for the glaze ice, Shin's data from [36].

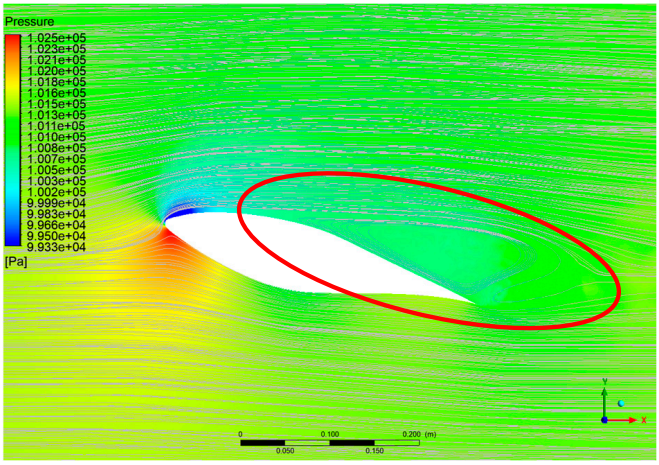

Figure 22. Glaze ice: pressure contours and streamlines at an AoA of 15°; beading model and Spalart–Allmaras model.

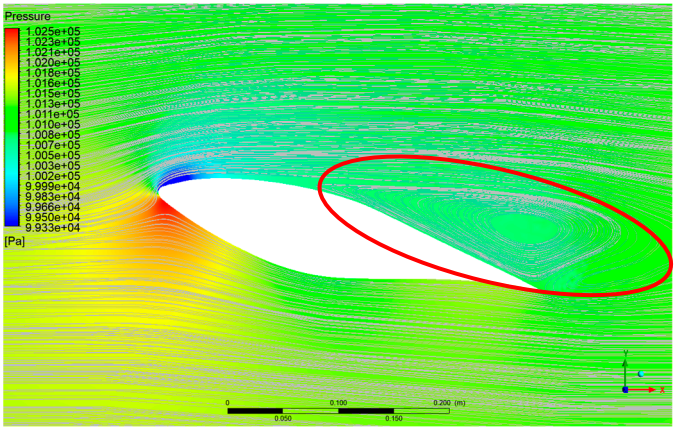

Figure 23. Glaze ice: pressure contours and streamlines at an AoA of 15°; Shin et al. [36] model and Spalart–Allmaras model.

Figures 24 and 25 show the behavior of the skin friction (C_f) and pressure (C_p) coefficients, respectively, in the iced configurations with glaze ice at an AoA of 15°. When comparing such coefficients with the clean profile scenario, the trends are similar to those observed with rime ice: the C_f peak at the leading edge is higher than in clean conditions

and C_p magnitude in the same position is lower than in the no-ice scenario, being even lower than in the case of rime ice (Figure 25). This observation is consistent with the lower C_L coefficients attained under glaze ice (Figure 20). In the case of the friction coefficient, shown in Figure 24, the separation points in the extrados are not so clearly identified as in the clean profile; the C_f curves show, for all the cases, a smooth decreasing shape reaching very low values already at 15% of the chord, suggesting a detached flow, as observed in Figures 22 and 23. As for rime ice, both turbulence models provide very similar results for both coefficients, with the differences mainly located in the area between the leading edge and 20% of the chord. Here, the C_p and C_f predicted by the SA model are somewhat higher than those provided by the k-ω SST model.

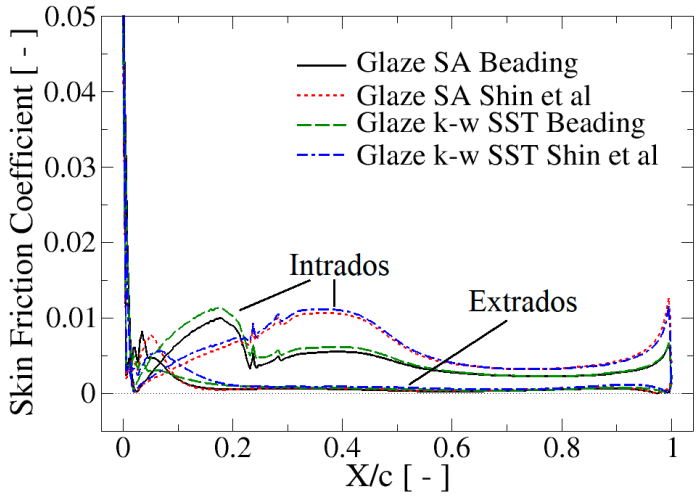

Figure 24. Glaze ice: skin friction coefficient at an AoA of 15° of the iced profile with both turbulence and roughness models, Shin's data from [36].

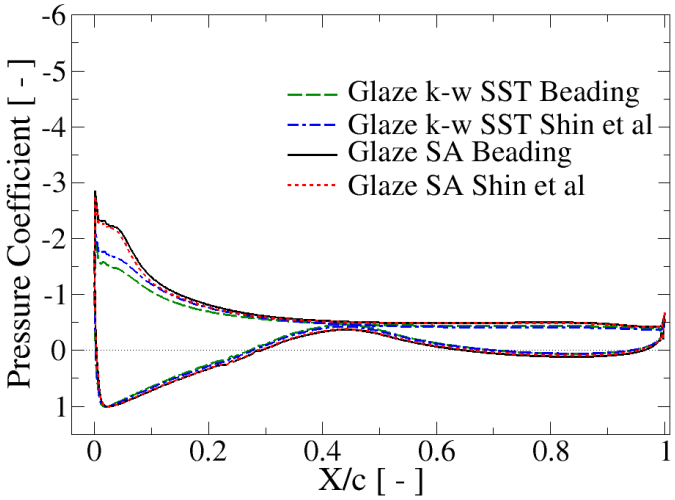

Figure 25. Glaze ice: pressure coefficient at an AoA of 15° of the clean profile with both turbulence and roughness models, Shin's data from [36].

The influence on the same coefficients of the roughness model can also be seen in Figures 24 and 25. Apparently, C_p is only slightly modified by the roughness model, being noticeable only in the leading 20% of the chord in the profile extrados for the k-ω SST model. However, differences are more obvious in the skin friction coefficient. In the intrados, similar to what happened with rime ice, the secondary maximum of C_f predicted by the Shin et al. model is close to 40% of the chord, while the beading model predicts a bump near the leading edge with a maximum of around 20% of the chord; the extent of

such a bump coincides with the region of the profile contaminated with ice (see Figure 26). In the extrados, the Shin et al. [36] model predicts higher values of C_f than the beading model, except perhaps in the area very close to the leading edge. In summary, it can be stated that the Shin et al. model provides higher values of the skin friction coefficient than the beading model; however, the last one can concentrate the friction effects on the area where the ice is deposited, while the first model distributes such an influence along the whole profile. In this sense, it can be argued that the beading model responds better to the physics of the problem than the Shin et al. [36] model, at least for the present application to wind turbine profiles.

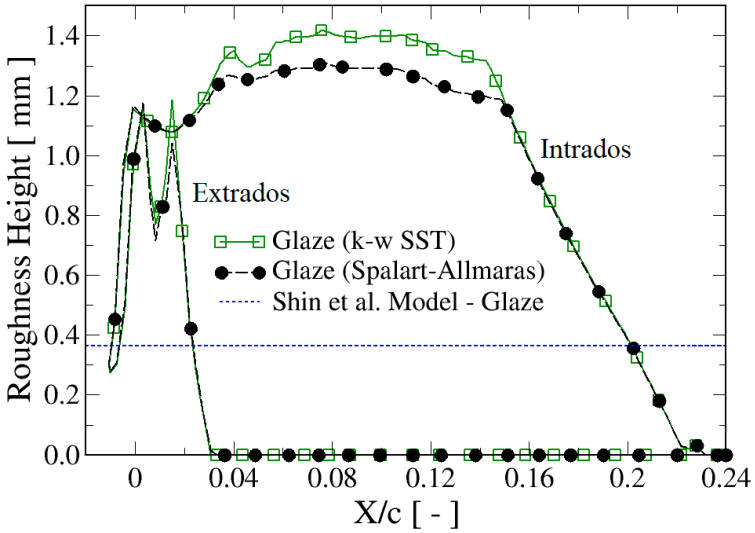

Figure 26. Distribution of the roughness height along the S809 airfoil for glaze ice at an AoA of 15°, Shin's data from [36].

As shown in Figure 26, the roughness estimated by the beading model in the case of glaze ice affects approximately 24% of the airfoil. As seen from that figure, the roughness estimated with the Spalart–Allmaras model is lower than that estimated by the k-ω SST model (around 8%). On the contrary, the Shin et al. model predicts a uniform roughness along the profile with a very similar value to the case of rime ice.

Using the beading model (see Table 7), it was found that for angles of attack of 0° and 10°, the loss in lift coefficient using both turbulence models was less than 7%. For the angle of attack of 5°, a 3.5% increase in the lift coefficient was obtained with the two turbulence models. However, at 15°, there was a loss of 36.71% with the Spalart–Allmaras model and 44.65% with the k-ω SST model. The average loss in the lift coefficient was 15.10% using the k-ω SST model and 12.80% using the Spalart–Allmaras model. As in the rime ice conditions, the drag coefficient followed the expected behavior, increasing monotonically with the angle of attack, reaching its maximum at 15°. Again, the highest increase was estimated by the Spalart–Allmaras model, with an average value of 59.34%.

Table 7. Aerodynamic loss estimated using the beading model with glaze ice.

	Clean				**Iced (Beading Model)**				**% Difference (Iced vs. Clean)**			
	Spalart–Allmaras		**k-ω SST**		**Spalart–Allmaras**		**k-ω SST**		**Spalart–Allmaras**		**k-ω SST**	
AOA (°)	**C_L**	**C_D**	**C_L**	**C_D**	**C_L**	**C_D**	**C_L**	**C_D**	**C_L**	**C_D**	**C_L**	**C_D**
0	0.124	0.012	0.123	0.013	0.117	0.015	0.116	0.015	−5.80%	18.25%	−6.04%	19.46%
5	0.632	0.015	0.639	0.016	0.653	0.018	0.663	0.018	3.32%	20.08%	3.55%	20.68%
10	1.106	0.026	1.029	0.029	1.047	0.041	0.966	0.041	−5.39%	61.91%	−6.15%	48.20%
15	1.284	0.065	1.129	0.069	0.812	0.153	0.625	0.153	−36.71%	137.12%	−44.65%	119.05%
				Average:					−12.80%	59.34%	−15.10%	51.85%

The results obtained with the Shin et al. model in the wet regime are presented in Table 8 and follow similar trends as in rime ice. In this case, the average drop in the lift coefficient in the ice scenario is around 19% with the SA model and 23% in the k-ω SST model. A slight increase of about 2% in C_L is predicted for an AoA of 5°, similar to what happened with the beading model. At the same time, C_D increases with mean increments of around 94% and 83% for the one and two equation turbulence models.

Table 8. Aerodynamic loss estimated using the Shin et al. [36] model with glaze ice.

	Clean				Iced (Shin et al. Model)				% Difference (Iced vs. Clean)			
	Spalart–Allmaras		k-ω SST		Spalart–Allmaras		k-ω SST		Spalart–Allmaras		k-ω SST	
AOA (°)	C_L	C_D	C_L	C_D	C_L	C_D	C_L	C_D	C_L	C_D	C_L	C_D
0	0.124	0.012	0.123	0.013	0.092	0.021	0.089	0.023	−25.39%	72.10%	−29.98%	72.81%
5	0.632	0.015	0.639	0.016	0.643	0.026	0.656	0.028	1.85%	70.89%	2.47%	71.71%
10	1.106	0.026	1.029	0.029	1.005	0.049	0.844	0.053	−9.12%	93.16%	−18.05%	78.95%
15	1.284	0.065	1.129	0.069	0.778	0.154	0.661	0.145	−39.37%	138.91%	−41.44%	109.14%
				Average:					−18.93%	93.77%	−22.98%	83.15%

In general, the Shin et al. model predicts lower C_L and higher C_D than the beading model, which is the same trend as in rime ice. Again, this difference is mainly attributed to the airfoil area covered by ice (see Figures 12 and 26). On the other hand, the trends of the influence of the ice roughness model on the aerodynamic performance of the S809 airfoil are very similar for both turbulence models, SA and k-ω SST (see Tables 7 and 8). This fact, together with the curves of C_f and C_p shown in Figures 24 and 25, means that, in terms of the simulation outcomes, the modeling of ice-induced roughness is more critical than the election of turbulence model.

4.3. Analysis of the Aerodynamic Performance of the Iced Airfoils

As anticipated, ice on the S809 profile reduced the lift coefficient under both regimes, rime and glaze (Figures 13 and 20), while C_D increased (Figures 14 and 21). This agrees with the results in the literature [12,29,48,57,58]. The following tables compare the aerodynamic coefficients between the different ice scenarios considering the roughness and turbulence models employed.

The average difference in the lift coefficient (see Table 9) between the dry regime and the wet regime using the beading model was 7.67% with the k-ω SST model and 3.66% with the Spalart–Allmaras model, indicating a variation between the two turbulence models of less than 5%. However, for an angle of attack of 15°, the Spalart–Allmaras model estimates a gain in the lift coefficient of 8.63%, while the k-ω SST model estimates a loss of 24.41%. This difference can be attributed to the limitations of the Spalart–Allmaras model under adverse pressure gradient conditions.

Table 9. Lift coefficient comparison of regimes using the beading model.

AoA (°)	k-ω SST Model			Spalart–Allmaras Model		
	C_L Rime	C_L Glaze	% Diff	C_L Rime	C_L Glaze	% Diff
0	0.120	0.116	−3.97%	0.121	0.117	−3.99%
5	0.662	0.663	0.11%	0.652	0.653	0.18%
10	0.988	0.966	−2.20%	1.066	1.047	−1.84%
15	0.827	0.625	−24.41%	0.748	0.812	8.63%
Average			7.67%			3.66%

The average difference in the drag coefficient (see Table 10) was higher, 18.78% with the k-ω SST and 11.97% with the Spalart–Allmaras models, indicating a difference between the two turbulence models of less than 7%. This increase in C_D is expected since the surface of the airfoil covered by ice was 5% greater in the wet regime than in the dry regime.

Table 10. Drag coefficient comparison of regimes using the beading model.

AoA (°)	k-ω SST Model			Spalart–Allmaras Model		
	C_D Rime	C_D Glaze	% Diff	C_D Rime	C_D Glaze	% Diff
0	0.015	0.016	9.92%	0.013	0.015	10.80%
5	0.018	0.020	9.10%	0.017	0.018	10.36%
10	0.037	0.044	17.27%	0.034	0.041	22.96%
15	0.110	0.152	38.83%	0.148	0.153	3.77%
Average			18.78%			11.97%

The average difference in the lift coefficient (Table 11) between the dry and wet regimes using the Shin et al. [36] model was 4.91% with the k-ω SST model and 2.25% with the Spalart–Allmaras model. The average difference in the drag coefficient (see Table 12) was slightly higher, being 8.89% with the k-ω SST model and 6.78% with the Spalart–Allmaras model. In these cases, the difference between the turbulence models was less than 3%. Similar findings were reported by Martini et al. [12] for a different airfoil (NACA 64-618).

Table 11. Lift coefficient comparison of regimes using the Shin et al. model.

AoA (°)	k-ω SST Model			Spalart–Allmaras Model		
	C_L Rime	C_L Glaze	% Diff	C_L Rime	C_L Glaze	% Diff
0	0.089	0.086	−3.65%	0.095	0.092	−3.15%
5	0.652	0.656	0.60%	0.638	0.643	0.80%
10	0.851	0.844	−0.87%	1.000	1.005	0.54%
15	0.774	0.661	−14.53%	0.815	0.778	−4.52%
Average			4.91%			2.25%

Table 12. Drag coefficient comparison of regimes using the Shin et al. [36] model.

AoA (°)	k-ω SST Model			Spalart–Allmaras Model		
	C_D Rime	C_D Glaze	% Diff	C_D Rime	C_D Glaze	% Diff
0	0.023	0.023	0.06%	0.022	0.022	−0.14%
5	0.028	0.028	2.21%	0.025	0.026	2.36%
10	0.049	0.053	7.84%	0.045	0.049	9.13%
15	0.116	0.146	25.46%	0.134	0.155	15.48%
Average			8.89%			6.78%

As can be observed from the previous values, the predictions of aerodynamic characteristics by the Shin et al. [36] model are less sensitive to the type of ice regime than those by the beading model, presenting lower variations in both the lift and drag coefficients.

Regarding the ice type, the present results indicate that the wet regime negatively impacts the aerodynamic performance of the airfoil. Comparing the aerodynamic coefficients of the airfoil evaluated under glaze ice versus the clean airfoil, the lift loss using the k-ω SST model and the beading model was 6% higher than that obtained with the rime ice (compare values in Tables 5 and 7). In contrast, with the Shin et al. model, the increase was 3.48% (compare values in Tables 6 and 8). However, when evaluating the Spalart–Allmaras model, the increase in lift loss between the two regimes using either roughness model was less than 2%. In the case of the drag coefficient, the difference between the regimes was more evident.

Regarding the combination of k-ω SST and the beading model, the increase was 25.99% (compare values in Tables 5 and 7), while with the Shin et al. [36] model, it was 14.82% (compare values in Tables 6 and 8). As with the lift coefficient, the increase was lower using the Spalart–Allmaras model, 15.41% combined with the beading model and 12.97% with

the Shin et al. [36] model. The above affirms that the airfoil performance will be more affected under conditions of glaze ice.

The combination of the k-ω SST turbulence model and the Shin et al. [36] model for the roughness modeling generated the highest loss of lift coefficient for both regimes (19.50% for rime ice and 22.98% for glaze ice). Similar findings were reported by Martini et al. [12] for a NACA 64-618 airfoil where the C_L loss was 22.54% under rime ice conditions. The combination of the Spalart–Allmaras turbulence model and the Shin et al. model generated the highest drag coefficient increase for both regimes (80.80% for rime ice and 93.77% for glaze ice). The findings reported by Martini et al. [12] under rime ice using the same models are notably higher, with some exceeding 120%. Differences in the airfoil design can account for these variations. For instance, the S809 profile has been specifically designed to obtain lower drag coefficients and maximum lift and to be insensitive to roughness [46]. The clean airfoil yielded comparable outcomes with a slight discrepancy in drag estimation at a 15° angle of attack when employing both turbulence models. This variation is attributed to the proximity to conditions of flow separation on the airfoil's suction side. As previously explained, the Spalart–Allmaras turbulence model exhibits limitations in boundary layer separation scenarios, which are accentuated when ice accumulates on the airfoil.

A related study was carried out by Caccia and Guardone [37], in which the authors searched to verify whether the negative effect on the aerodynamic performance of the profiles was due to the ice shape or the roughness. The roughness model of Shin et al. was employed in [37], and the model known as Wright's relation, which was determined from experimental measurements of the roughness height as a function of the freezing fraction at the stagnation point. The analysis was performed only for the dry regime (freezing fraction equal to 1) in different sections of the NREL 5MW turbine blade [59] composed at the base by DU profiles and, at the tip, by NACA 643-618 profiles. Using the Spalart–Allmaras turbulence model, the roughness values were evaluated in two ways: the first one only in the area where ice accumulated (similar to what the FENSAP-ICE beading model does) and the second one at 0.44 m along the leading edge of the profile on both the suction and pressure sides. Caccia and Guardone [37] found that ice caused a degradation in profile aerodynamic performance in all the evaluated cases due to both ice shape and roughness. Regarding the ice shape, the icing condition evaluated generated a "horn" on the leading edge of the NACA 643-618 profiles. In contrast, in the DU profiles, the ice followed the shape of the profile. This horn shape produced a significant decrease in the performance of the NACA profiles. In the case of roughness, the effect of the extent of roughness and the value of its height became more critical as the angle of attack increased.

From the results presented in the previous sections and the performed discussions, it is seen that there is a close agreement between the attained conclusions in the present study and those of Caccia and Guardone [37], i.e., the stall was anticipated, the lift coefficient slope decreased, and the drag coefficient increased in the case of iced airfoil. Furthermore, both studies found that the most significant difference occurred when the roughness height was higher and covered a larger airfoil area. The present results extend the same conclusions for the glaze ice scenario.

5. Conclusions

This study examines the impact of two surface roughness models, combined with two turbulence models, on the aerodynamic performance of the S809 wind turbine airfoil during rime and glaze ice via CFD simulation with FENSAP-ICE software. It has been shown that computational results of the aerodynamic parameters and ice shape were in reasonable agreement with the experimental and numerical data for clean and iced airfoils. The main conclusions of the study are summarized as follows:

1. Iced airfoil analysis revealed increased drag and reduced lift, consistent with the literature. Under the rime ice condition, C_D increased by around 50%, and C_L decreased by approximately 15%. These aerodynamic coefficients showed a higher

impact in the glaze ice condition, increasing to 70% for C_D and decreasing to 20% for C_L, emphasizing the need for further investigation into glaze ice conditions.

2. The modification of the airfoil lift and drag characteristics in the presence of ice is explained by the behavior of the skin friction and pressure coefficients. The occurrence of the ice layer and its induced roughness promotes an alteration in the pressure and wall shear stress around the profile, which increases skin friction and decreases the pressure coefficient. Also, it has been shown that the airfoil experiences an earlier flow separation with accreted ice compared to clean conditions, with the effect of increasing drag and reducing lift.
3. On the other hand, the turbulence model selection did not significantly affect outcomes for aerodynamic coefficients. Average differences were around 3% for rime ice conditions and 2% for glaze ice conditions.
4. However, surface roughness was crucial, requiring consideration at each growth stage during ice accretion simulations. Validation of data obtained with experiments is recommended to determine which roughness model yields better results.
5. The beading model has shown excellent handling of the roughness variation along the ice accretion process. However, further validation of the model is needed to evaluate accuracy fully.
6. The widely used Shin et al. model may underestimate the lift coefficient and overestimate the drag coefficient compared to the beading model, suggesting that the first, which assumes that roughness is uniformly distributed along the entire airfoil, does not accurately reflect the actual physical nature of roughness distribution in the wind turbine simulated conditions.
7. Accurate predictions cannot rely solely on empirical correlations from the aeronautics domain. In this context, on-site roughness measurements are imperative to eliminate uncertainties.

The validated modeling methods and simulation utilities presented in this research would benefit scholars and engineers conducting reliable simulations for icing on wind turbine blades. However, it is essential to emphasize that the analysis was limited to two-dimensional aerodynamic performance; future analyses should be carried out to understand the effect of icing from a three-dimensional point of view that includes other phenomena, such as the influence of airflow along the blade span induced by its rotation.

Author Contributions: Conceptualization, L.T.C.M. and A.I.; methodology, L.T.C.M. and S.L.; software, L.T.C.M.; validation, L.T.C.M.; formal analysis, L.T.C.M., A.I. and S.L.; data curation, L.T.C.M.; writing—original draft preparation, L.T.C.M.; writing—review and editing, A.I. and S.L.; supervision, A.I. and S.L. All authors have read and agreed to the published version of the manuscript.

Funding: This research received no external funding.

Data Availability Statement: Data are contained within the article.

Acknowledgments: Special acknowledgment to Nergica for the data provided.

Conflicts of Interest: The authors declare no conflict of interest.

References

1. O'Brien, J.M.; Young, T.M.; O'Mahoney, D.C.; Griffin, P.C. Horizontal axis wind turbine research: A review of commercial CFD, FE codes and experimental practices. *Prog. Aerosp. Sci.* **2017**, *92*, 1–24. [CrossRef]
2. Han, W.; Kim, J.; Kim, B. Study on correlation between wind turbine performance and ice accretion along a blade tip airfoil using CFD. *J. Renew. Sustain. Energy* **2018**, *10*, 023306. [CrossRef]
3. Pedersen, M.C.; Sørensen, H. Towards a CFD Model for Prediction of Wind Turbine Power Losses due to Icing in Cold Climate. In Proceedings of the 16th International Symposium on Transport Phenomena and Dynamics of Rotating Machinery, Honolulu, HI, USA, 10–15 April 2016; p. 7.
4. Fei, C.-W.; Han, Y.-J.; Wen, J.-R.; Li, C.; Han, L.; Choy, Y.-S. Deep learning-based modeling method for probabilistic LCF life prediction of turbine blisk. *Propuls. Power Res.* **2023**. [CrossRef]
5. Chen, J.-Y.; Feng, Y.-W.; Teng, D.; Lu, C.; Fei, C.-W. Support vector machine-based similarity selection method for structural transient reliability analysis. *Reliab. Eng. Syst. Saf.* **2022**, *223*, 108513. [CrossRef]

6. Hacıefendioğlu, K.; Başağa, H.B.; Yavuz, Z.; Karimi, M.T. Intelligent ice detection on wind turbine blades using semantic segmentation and class activation map approaches based on deep learning method. *Renew. Energy* **2022**, *182*, 1–16. [CrossRef]
7. Fakorede, O.; Feger, Z.; Ibrahim, H.; Ilinca, A.; Perron, J.; Masson, C. Ice protection systems for wind turbines in cold climate: Characteristics, comparisons and analysis. *Renew. Sustain. Energy Rev.* **2016**, *65*, 662–675. [CrossRef]
8. Hu, L.; Zhu, X.; Hu, C.; Chen, J.; Du, Z. Wind turbines ice distribution and load response under icing conditions. *Renew. Energy* **2017**, *113*, 608–619. [CrossRef]
9. Hu, L.; Zhu, X.; Chen, J.; Shen, X.; Du, Z. Numerical simulation of rime ice on NREL Phase VI blade. *J. Wind Eng. Ind. Aerodyn.* **2018**, *178*, 57–68. [CrossRef]
10. Rizk, P.; Younes, R.; Ilinca, A.; Khoder, J. Wind turbine ice detection using hyperspectral imaging. *Remote Sens. Appl. Soc. Environ.* **2022**, *26*, 100711. [CrossRef]
11. Laín, S.; Contreras, L.T.; López, O. A review on computational fluid dynamics modeling and simulation of horizontal axis hydrokinetic turbines. *J. Braz. Soc. Mech. Sci. Eng.* **2019**, *41*, 375. [CrossRef]
12. Martini, F.; Ibrahim, H.; Contreras Montoya, L.T.; Rizk, P.; Ilinca, A. Turbulence Modeling of Iced Wind Turbine Airfoils. *Energies* **2022**, *15*, 8325. [CrossRef]
13. Etemaddar, M.; Hansen, M.O.L.; Moan, T. Wind turbine aerodynamic response under atmospheric icing conditions. *Wind Energy* **2014**, *17*, 241–265. [CrossRef]
14. Villalpando, F.; Reggio, M.; Ilinca, A. Prediction of ice accretion and anti-icing heating power on wind turbine blades using standard commercial software. *Energy* **2016**, *114*, 1041–1052. [CrossRef]
15. Jin, J.Y.; Virk, M.S. Study of ice accretion along symmetric and asymmetric airfoils. *J. Wind Eng. Ind. Aerodyn.* **2018**, *179*, 240–249. [CrossRef]
16. Jin, J.Y.; Virk, M.S. Study of ice accretion and icing effects on aerodynamic characteristics of DU96 wind turbine blade profile. *Cold Reg. Sci. Technol.* **2019**, *160*, 119–127. [CrossRef]
17. Yirtici, O.; Cengiz, K.; Ozgen, S.; Tuncer, I.H. Aerodynamic validation studies on the performance analysis of iced wind turbine blades. *Comput. Fluids* **2019**, *192*, 104271. [CrossRef]
18. Yirtici, O.; Ozgen, S.; Tuncer, I.H. Predictions of ice formations on wind turbine blades and power production losses due to icing. *Wind Energy* **2019**, *22*, 945–958. [CrossRef]
19. Pedersen, M.C. Modelling Icing on Structures for Wind Power Applications. Ph.D. Dissertation, Aalborg University, Aalborg, Denmark, 2018.
20. Shu, L.; Li, H.; Hu, Q.; Jiang, X.; Qiu, G.; He, G.; Liu, Y. 3D numerical simulation of aerodynamic performance of iced contaminated wind turbine rotors. *Cold Reg. Sci. Technol.* **2018**, *148*, 50–62. [CrossRef]
21. Jin, J.Y.; Virk, M.S.; Hu, Q.; Jiang, X. Study of Ice Accretion on Horizontal Axis Wind Turbine Blade Using 2D and 3D Numerical Approach. *IEEE Access* **2020**, *8*, 166236–166245. [CrossRef]
22. IEA Wind. *Wind Energy in Cold Climates Available Technologies—Report*; VTT Technical Research Centre on Finland Ltd.: Tampere, Finland, 2016; p. 120.
23. Pedersen, M.C.; Yin, C. Preliminary Modelling Study of Ice Accretion on Wind Turbines. *Energy Procedia* **2014**, *61*, 258–261. [CrossRef]
24. Contreras Montoya, L.T.; Lain, S.; Ilinca, A. A Review on the Estimation of Power Loss Due to Icing in Wind Turbines. *Energies* **2022**, *15*, 1083. [CrossRef]
25. ANSYS Inc. In-Flight Icing Simulation. Available online: https://www.ansys.com/products/fluids/ansys-fensap-ice (accessed on 10 November 2022).
26. Hann, R.; Hearst, R.J.; Sætran, L.R.; Bracchi, T. Experimental and Numerical Icing Penalties of an S826 Airfoil at Low Reynolds Numbers. *Aerospace* **2020**, *7*, 46. [CrossRef]
27. Knobbe-Eschen, H.; Stemberg, J.; Abdellaoui, K.; Altmikus, A.; Knop, I.; Bansmer, S.; Balaresque, N.; Suhr, J. Numerical and experimental investigations of wind-turbine blade aerodynamics in the presence of ice accretion. In Proceedings of the AIAA Scitech 2019 Forum, San Diego, CA, USA, 7–11 January 2019.
28. Li, Y.; Wang, S.; Sun, C.; Yi, X.; Guo, W.; Zhou, Z.; Feng, F. Icing distribution of rotating blade of horizontal axis wind turbine based on Quasi-3D numerical simulation. *Therm. Sci.* **2018**, *22*, 681–691. [CrossRef]
29. Homola, M.C.; Virk, M.S.; Nicklasson, P.J.; Sundsbø, P.A. Performance losses due to ice accretion for a 5 MW wind turbine. *Wind Energy* **2012**, *15*, 379–389. [CrossRef]
30. Makkonen, L.; Laakso, T.; Marjaniemi, M.; Finstad, K.J. Modelling and Prevention of Ice Accretion on Wind Turbines. *Wind Eng.* **2001**, *25*, 3–21. [CrossRef]
31. Virk, M.; Mughal, U.; Hu, Q.; Jiang, X. Multiphysics Based Numerical Study of Atmospheric Ice Accretion on a Full Scale Horizontal Axis Wind Turbine Blade. *Int. J. Multiphys.* **2016**, *10*, 237–246. [CrossRef]
32. Fu, P.; Farzaneh, M. A CFD approach for modeling the rime-ice accretion process on a horizontal-axis wind turbine. *J. Wind Eng. Ind. Aerodyn.* **2010**, *98*, 181–188. [CrossRef]
33. Bai, C.-J.; Wang, W.-C. Review of computational and experimental approaches to analysis of aerodynamic performance in horizontal-axis wind turbines (HAWTs). *Renew. Sustain. Energy Rev.* **2016**, *63*, 506–519. [CrossRef]
34. Menter, F. Zonal Two Equation k-w Turbulence Models For Aerodynamic Flows. In Proceedings of the 23rd Fluid Dynamics, Plasmadynamics, and Lasers Conference, Orlando, FL, USA, 6–9 July 1993.

35. Sagol, E.; Reggio, M.; Ilinca, A. Assessment of Two-Equation Turbulence Models and Validation of the Performance Characteristics of an Experimental Wind Turbine by CFD. *ISRN Mech. Eng.* **2012**, *2012*, 428671. [CrossRef]
36. Shin, J.; Berkowitz, B.; Chen, H.; Cebeci, T. Prediction of ice shapes and their effect on airfoil performance. In Proceedings of the 29th Aerospace Sciences Meeting, Reno, NV, USA, 7–10 January 1991; p. 264.
37. Caccia, F.; Guardone, A. Numerical simulation of ice accretion on wind turbine blades: Are performance losses due to ice shape or surface roughness? *Wind Energy Sci.* **2023**, *8*, 341–362. [CrossRef]
38. ANSYS Inc. *ANSYS FENSAP-ICE 18.1 User Manual*; ANSYS Inc.: Canonsburg, PA, USA, 2017.
39. Hildebrandt, S.; Sun, Q. Evaluation of operational strategies on wind turbine power production during short icing events. *J. Wind Eng. Ind. Aerodyn.* **2021**, *219*, 104795. [CrossRef]
40. Blasco, P.; Palacios, J.; Schmitz, S. Effect of icing roughness on wind turbine power production. *Wind Energy* **2017**, *20*, 601–617. [CrossRef]
41. Turkia, V.; Huttunen, S.; Wallenius, T. Method for estimating wind turbine production losses due to icing. *VTT Tech. Res. Cent. Finl.* **2013**, *114*, 44.
42. Fortin, G.; Perron, J. Wind Turbine Icing and De-Icing. In Proceedings of the 47th AIAA Aerospace Sciences Meeting Including the New Horizons Forum and Aerospace Exposition, Orlando, FL, USA, 5–8 January 2009; Aerospace Sciences Meetings. American Institute of Aeronautics and Astronautics: Reston, VA, USA, 2009.
43. Sagol, E. Three Dimensional Numerical Prediction of Icing Related Power and Energy Losses on a Wind Turbine. Ph.D. Thesis, École Polytechnique de Montréal, PolyPublie Polytechnique Montréal, Montréal, QC, Canada, 2014.
44. Farzaneh, M. *Atmospheric Icing of Power Networks*, 1st ed.; Springer: Berlin/Heidelberg, Germany, 2008; p. 381.
45. Battisti, L. Aerodynamic Performances on Ice Contaminated Rotors. In *Wind Turbines in Cold Climates*, 1st ed.; Springer International Publishing: Cham, Switzerland, 2015; p. 341.
46. Somers, D.M. *Design and Experimental Results for the S809 Airfoil*; National Renewable Energy Laboratory (NREL): Golden, CO, USA; U.S. Department of Energy, Office of Scientific and Technical Information: Oak Ridge, TN, USA, 1997.
47. Tan, H. CFD Analysis of a Wind Turbine Airfoil with Flap. Master's Thesis, Washinton University, St. Louis, MO, USA, 2020.
48. Han, Y.; Palacios, J.; Schmitz, S. Scaled ice accretion experiments on a rotating wind turbine blade. *J. Wind Eng. Ind. Aerodyn.* **2012**, *109*, 55–67. [CrossRef]
49. Hand, M.M.; Simms, D.A.; Fingersh, L.J.; Jager, D.W.; Cotrell, J.R.; Schreck, S.; Larwood, S.M. *Unsteady Aerodynamics Experiment Phase VI WindTunnel Test Configurations and Available Data Campaigns*; National Renewable Energy Laboratory—NREL: Golden, CO, USA, 2001; p. 310.
50. Li, Y.; Sun, C.; Jiang, Y.; Yi, X.; Zhang, Y. Effect of liquid water content on blade icing shape of horizontal axis wind turbine by numerical simulation. *Therm. Sci.* **2019**, *23*, 1637–1645. [CrossRef]
51. Burton, T.; Jenkins, N.; Sharpe, D.; Bossanyi, E. Aerodynamics of Horizontal Axis Wind Turbines. In *Wind Energy Handbook*; John Wiley & Sons, Inc.: Hoboken, NJ, USA, 2011; pp. 39–136.
52. Airfoil Tools. NREL's S809 Airfoil (s809-nr). Available online: http://airfoiltools.com/airfoil/details?airfoil=s809-nr (accessed on 5 February 2022).
53. Zanon, A.; De Gennaro, M.; Kühnelt, H. Wind energy harnessing of the NREL 5 MW reference wind turbine in icing conditions under different operational strategies. *Renew. Energy* **2018**, *115*, 760–772. [CrossRef]
54. Tardif d'Hamonville, T. Modélisation et Analyse des Phénomènes Aéroélastiques Pour Une Pale D'éolienne. Master's Thesis, Université du Québec à Chicoutimi, Chicoutimi, QC, Canada, 2009.
55. Hudecz, A.; Koss, H.; Laver, M.O. Ice Accretion on Wind Turbine Blades. In Proceedings of the 15th International Workshop on Atmospheric Icing of Structures (IWAIS XV), St. John's, NL, Canada, 8–13 September 2013; p. 8.
56. ANSYS Inc. *ANSYS Fluent User's Guide Release 15.0*; ANSYS Inc.: Canonsburg, PA, USA, 2013; p. 2692.
57. Bodenlle-Toral, D.; García-Regodeseves, P.; Pandal-Blanco, A. Performance evaluation of an airfoil under ice accretion using CFD simulations. *J. Phys. Conf. Ser.* **2022**, *2217*, 012088. [CrossRef]
58. Jasinski, W.J.; Noe, S.C.; Selig, M.S.; Bragg, M.B. Wind Turbine Performance Under Icing Conditions. *J. Sol. Energy Eng.* **1998**, *120*, 60–65. [CrossRef]
59. Jonkman, J.; Butterfield, S.; Musial, W.; Scott, G. *Definition of a 5-MW Reference Wind Turbine for Offshore System Development*; NREL/TP-500-38060; TRN: US200906%%69 United States 10.2172/947422 TRN: US200906%%69 NREL English; National Renewable Energy Lab. (NREL): Golden, CO, USA, 2009; p. 75.